EG2 Data-Mining Analysis Note: Inclusive (e,e') Cross-Section Measurements of the EMC Effect and the a_2 Plateau

Barak Schmookler

Massachusetts Institute of Technology

January 22, 2018

Contents

Chapter 1

Introduction

1.1 Motivation

In the simplest sense, the *European Muon Collaboration* (EMC) effect refers the observed non-unity of the per-nucleon lepton-inclusive Deep Inelastic Scattering (DIS) cross-section ratio of a nucleus A to Deuterium [1, 2]. The 'strength' of the EMC effect refers to the magnitude of the slope of the per-nucleon ratio between Bjorken-X or 0.3 and 0.7. This deviation from unity must originate from a difference in the internal quark-gluon structure of the nucleus A compared to Deuterium. Many theoretical models have been proffered to explain the EMC effect. Some models claim that all nucleons inside the nucleus are modified; while others focus on high-virtuality nucleons located in short-range correlated (SRC) pairs.

The number of SRC pairs in a nucleus A compared to Deuterium is also inferred from inclusive scattering, in this case from quasi-elastic (QE) scattering at Bjorken-X between 1.4 and 2 [3]. In this region, the per-nucleon cross-section ratio for a nucleus A to Deuterium shows a plateau. The value of this ratio in the plateau (a_2) is interpreted as the per-nucleon number of SRC pairs in the nucleus A relative to Deuterium.

The strength of the EMC effect has a strong linear correlation with a_2 for the six nuclei so far measured in both the DIS and QE regions, spanning from Helium to Gold[4, 5]. Thus, it is useful to extract EMC ratios and a_2 values for additional nuclei.

1.2   This Analysis

This analysis was performed on the *EG2c* dataset as part of the *CLAS* Data-Mining initiative [6]. The *EG2c* run period took place in 2004 using an electron beam with a nominal beam energy of 5.014 GeV [7, 8]. The experiment used a specially designed target cell consisting of a 2 cm long cryogenic cell (filled with either liquid Deuterium or liquid Hydrogen) as well as a solid target located approximately 5 cm downstream [9]. A mechanical lever arm allowed one of the six solid target foils (^{12}C, thick or thin ^{27}Al, ^{56}Fe, ^{118}Sn, or ^{208}Pb) to be remotely placed into the beam-line at a time.

The *EG2c* experiment operated with an open electron trigger design. This makes it possible to re-analyse the data, looking for physics not considered at the time the experiment was conducted. In this analysis, we present per-nucleon inclusive cross-section ratios for ^{12}C, ^{27}Al, ^{56}Fe, and ^{208}Pb to ^{2}D for both the Deep Inelastic Scattering (DIS) region and for high Bjorken-X Quasi-Elastic (QE) scattering.

Chapter 2

Event Reconstruction and Particle Selection

2.1 Electron Selection

2.1.1 Electron Particle Identification

In this analysis, we use the same electron particle identification (PID) cuts for both the DIS and QE analysis. This is justified because these exact same cuts were approved for an *EG2c* DIS analysis [10] and an *EG2c* QE analysis at high Bjorken-X [11]. In this analysis, we made sure to use the exact same cuts as for the approved analyses.

Nonetheless, we will give a brief overview of the applied cuts. Electrons candidate events are required to meet the following criteria: they must be the first row in the *EVNT* bank; they must leave a negatively charged track in the drift chamber; they must have corresponding hits in the scintillator, cherenkov, and calorimeter detectors.

To determine whether an electron candidate is in fact a good electron, a set of cuts is applied. First, as shown in figure 2.1, a minimum number of photoelectrons is required to be detected in the cherenkov counter. Second, the hit location in the calorimeter cannot be too close to the detector edge (figures 2.2 and 2.3). Next, a minimum energy is required to be deposited in both the inner and the outer layers of the calorimeter (figure 2.4). Finally, a correlation between the amount of energy deposited in each layer of the calorimeter and the momentum of the particle as determined by the drift chamber must be observed (figure 2.5). It is noted once more that these cuts

are the exact same ones used for the approved analyses [10, 11].
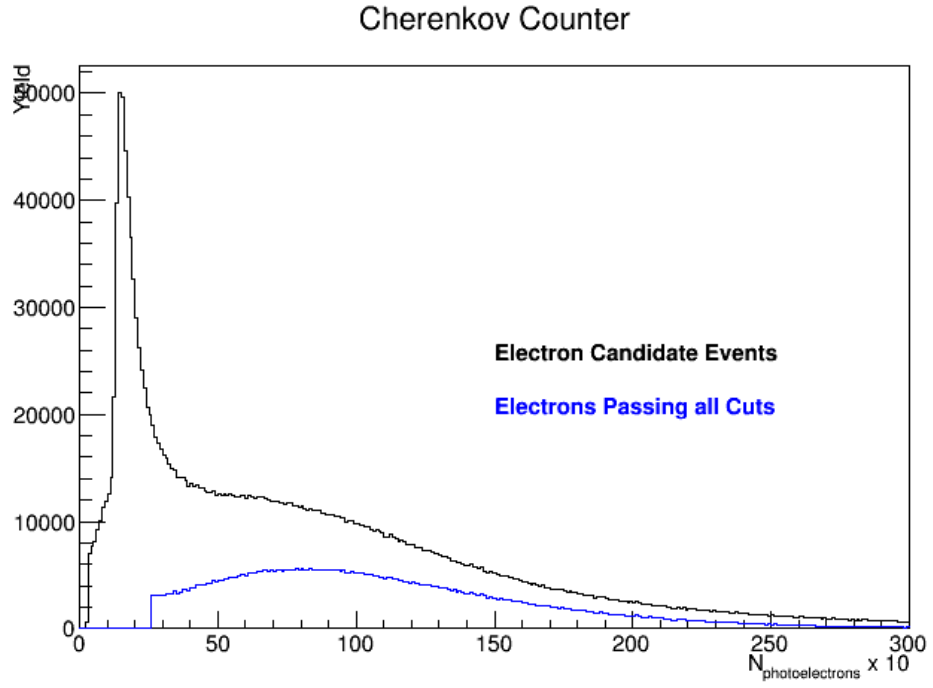
Figure 2.1: Number of photoelectrons deposited in the Cherenkov Counter.

Figure 2.2: Electromagnetic Calorimeter U, V, and W hit locations.

Figure 2.3: Electromagnetic Calorimeter X vs. Y hit locations.

Figure 2.4: Top: Energy deposited in electromagnetic calorimeter inner layer. Bottom: Energy deposited in electromagnetic calorimeter outer layer.

Figure 2.5: Momentum-Normalized energy deposited in the electromagnetic calorimeter. Top: Before PID Cuts. Bottom: After PID Cuts.

2.1.2 Electron Vertex Corrections

Since multiple targets were present in the beam-line for much of the *EG2c* run period, it is important to correctly recon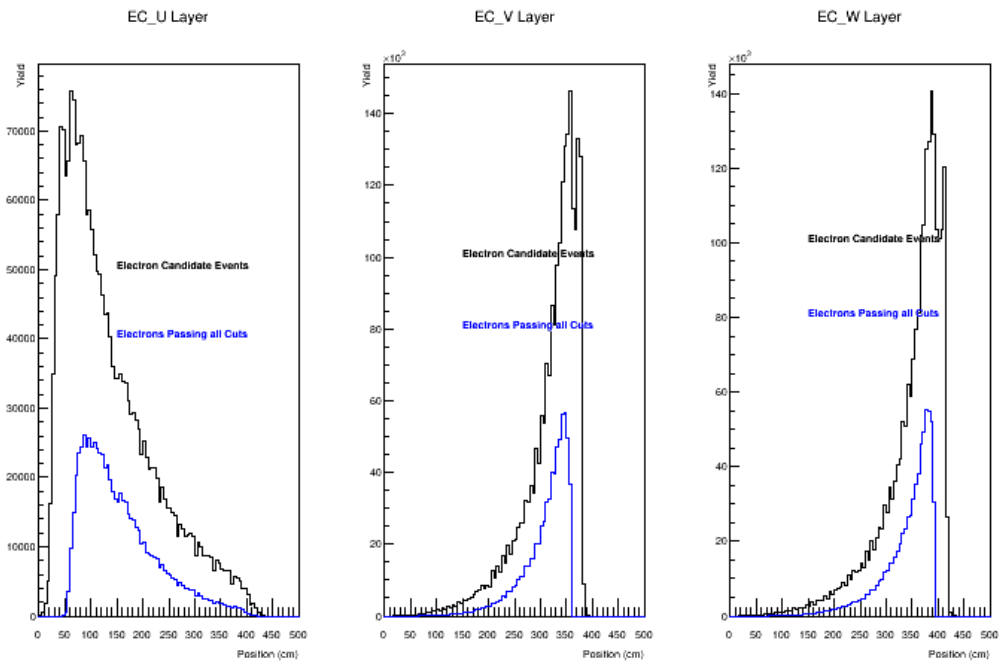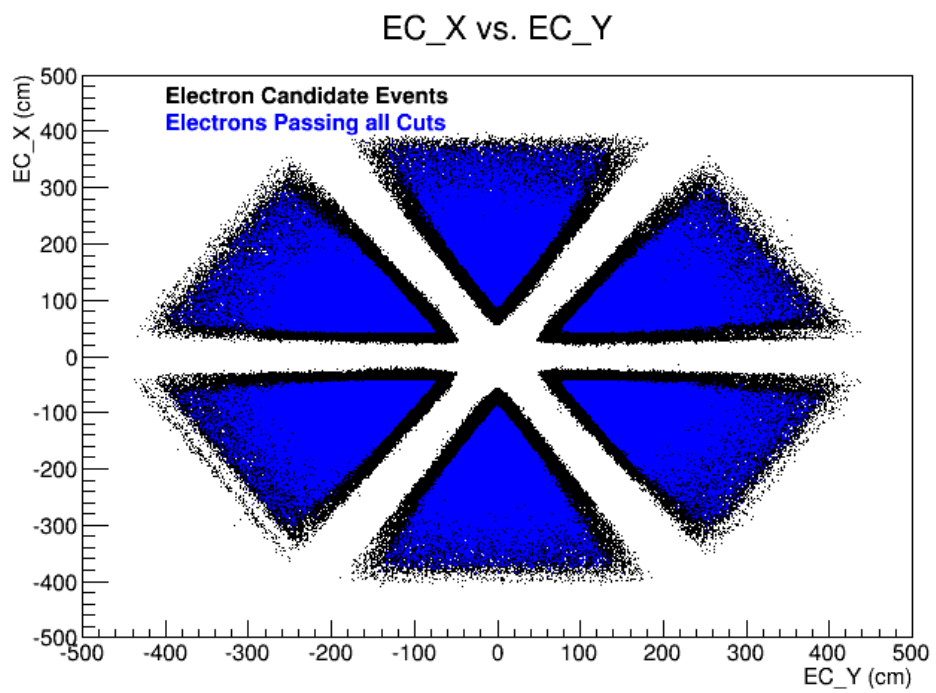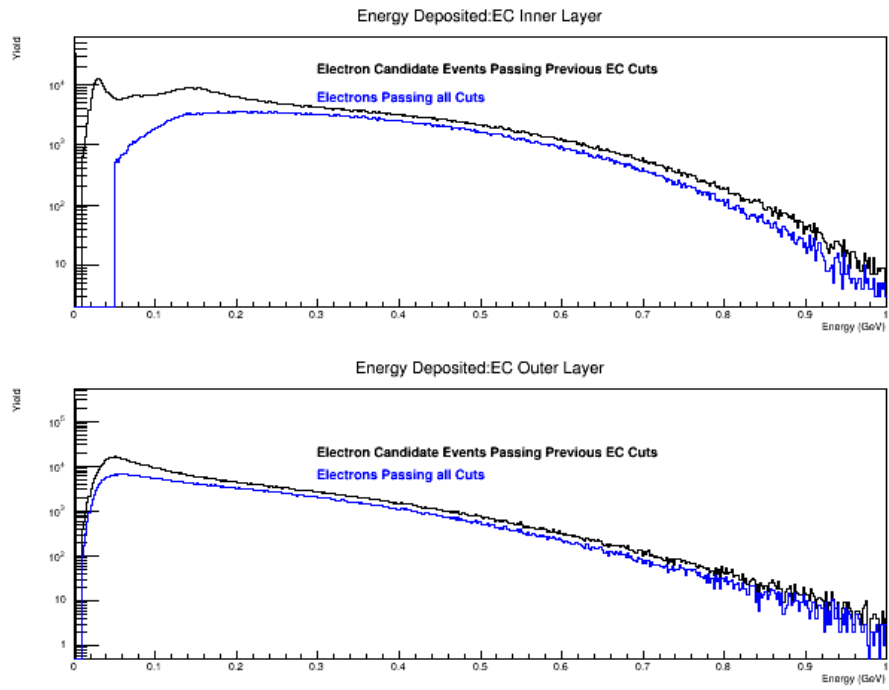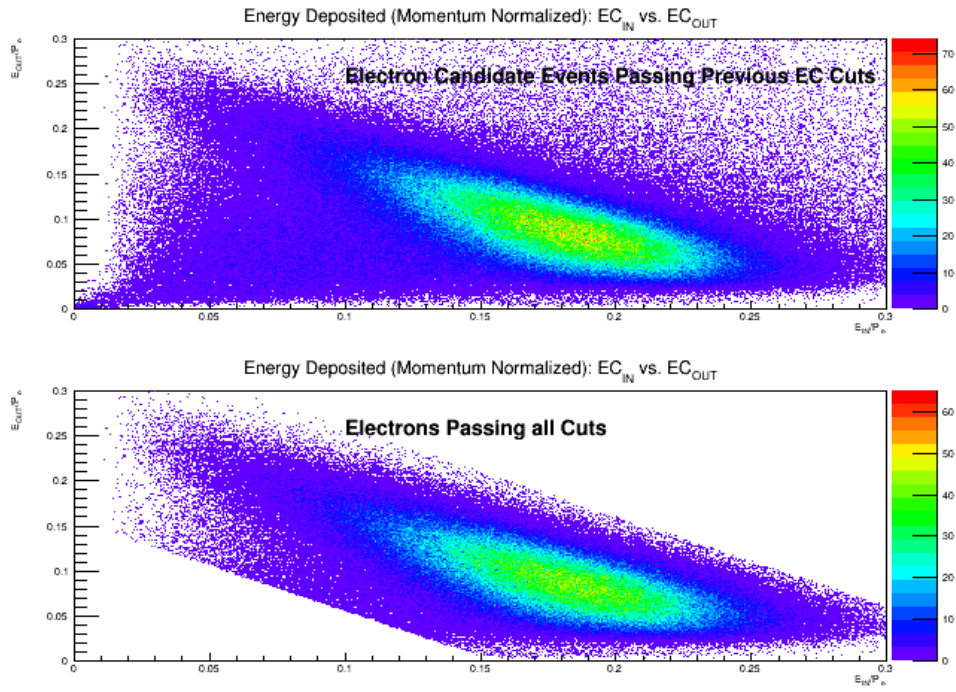struct the reaction vertex. If the electron beam is transversely offset from the ideal beam-line, the *CLAS* reconstruction software will reconstruct the reaction vertex incorrectly. (This offset will not affect the reconstructed momentum vectors). As discussed in reference [12], the vertex is incorrectly reconstructed in a known way, allowing for an easy correction. The reconstructed electron vertex for a Carbon/Deuterium run is shown in figure 2.6. The carbon foil should be located at -25 cm, but a clear sector-to-sector dependence is observed. In order to correct this, we follow the procedure in reference [12]. That is, we look at the reconstructed carbon foil vertex as a function of the azimuthal angle for a specific polar angle. Then we fit this dependence using the appropriate function, as shown in figure 2.7.
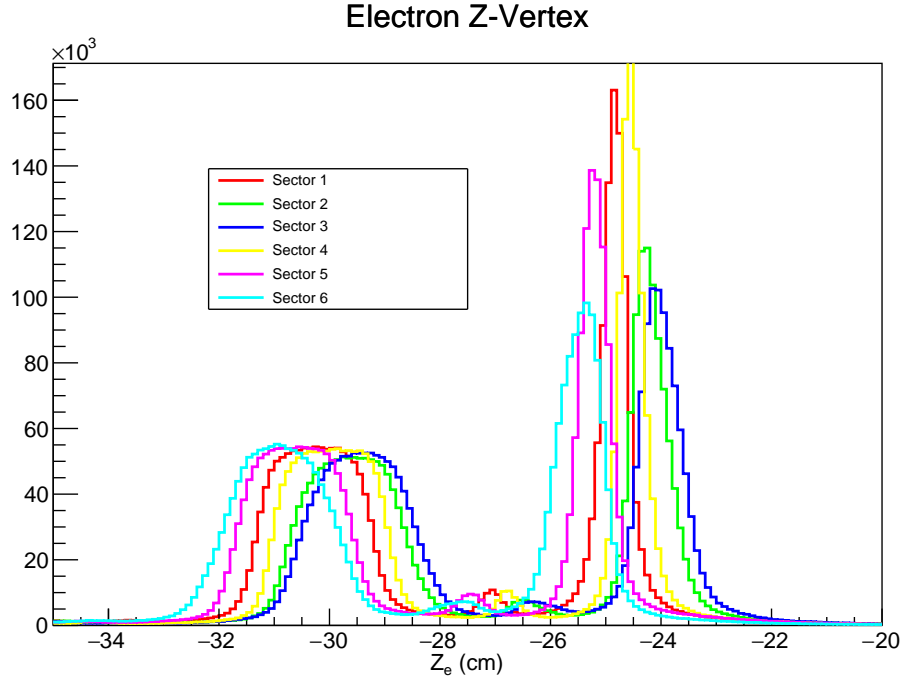

Figure 2.6: Reconstructed electron vertex for a Carbon/Deuterium run.

Although this fit describes the general features of the incorrect vertex reconstruction, there is still an issue within each sector. Our guess is that
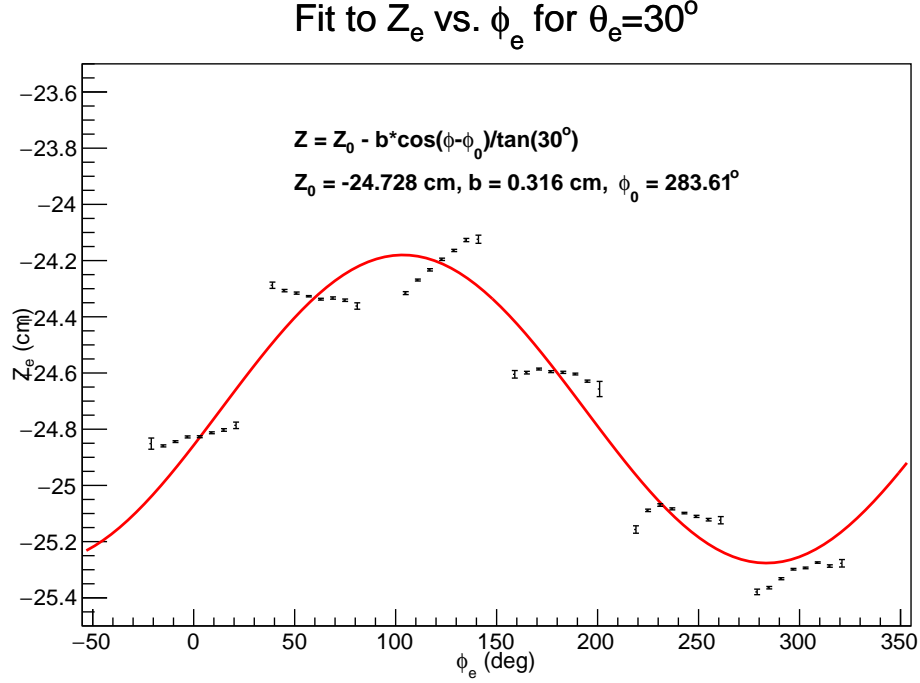
Figure 2.7: Sinusoidal fit (as described in reference [12]) to the carbon foil data. The data is fit at a fixed polar angle. We refer to the results of this fit in equations 2.1 and 2.2.

this has to do with the polar angle being not perfectly reconstructed (as described below). But, in any event, we developed the following ad-hoc procedure to correct the residuals. Noting that the true foil position is at -25 cm to the hall center, we can define two functions and write

$$\frac{True\,Vertex}{True\,Vertex - Fit\,Residual} = f(\phi) \times g(\theta) \qquad (2.1)$$

, where $f(\phi)$ and $g(\theta)$ are low (3rd) order polynomials. This extraction is justified in various momentum correction $CLAS$ notes [13]. First $f(\phi)$ is determined, as shown if figure 2.8; then, for every event, $g(\theta)$ is solved for in equation 2.1. This is plotted and fit as a function of θ, as shown if figure 2.9.

The upshot of all this is the creation of a corrected electron vertex. This corrected electron vertex is defined as
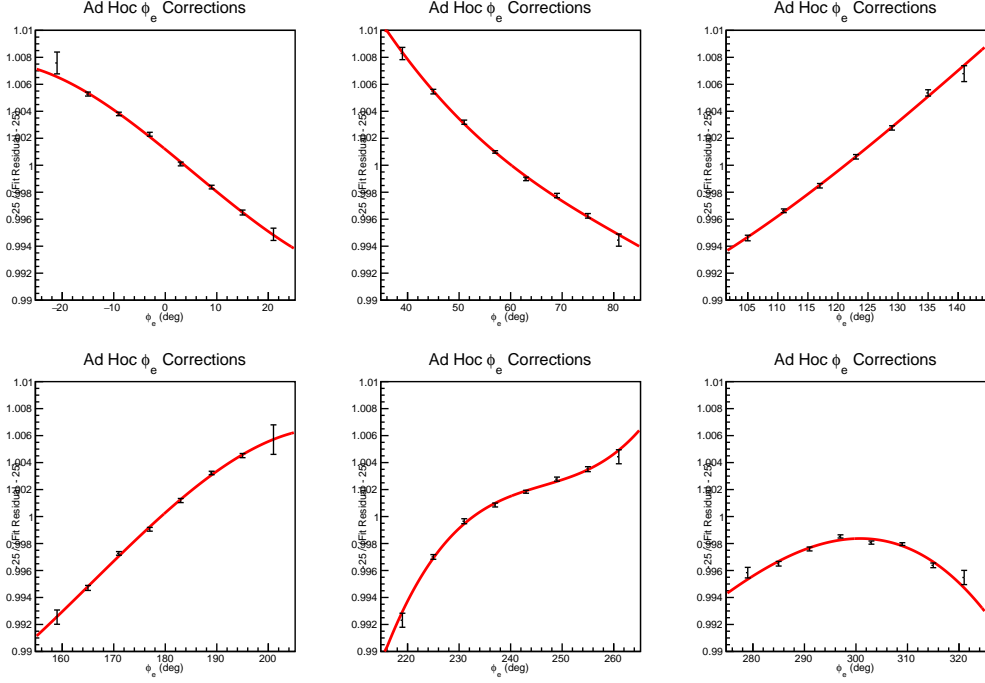
Figure 2.8: Determination of $f(\phi)$ for each sector. The functions ared 3rd degree polynomials.

$$Z_{corr} = (Z_{meas} + True\,Vertex - Fit) \times f(\phi) \times g(\theta) \qquad (2.2)$$

The corrected electron vertex is used for the remainder of the analysis. It is plotted in figures 2.10 - 2.12.

13
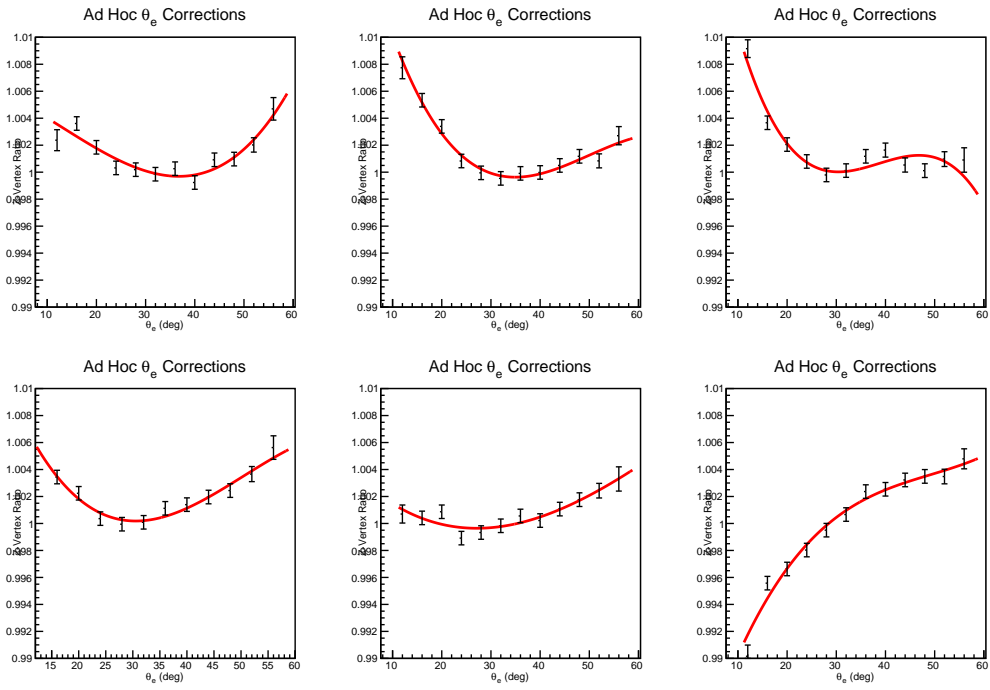
Figure 2.9: Determination of $g(\theta)$ for each sector. The functions are 3rd degree polynomials.

14
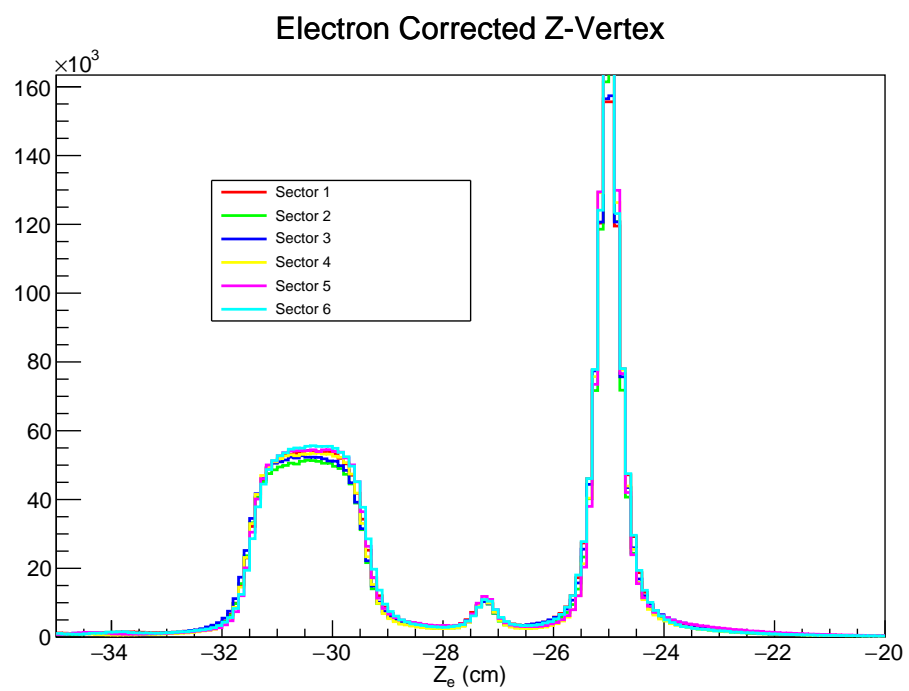
Figure 2.10: Plot of corrected electron vertex.
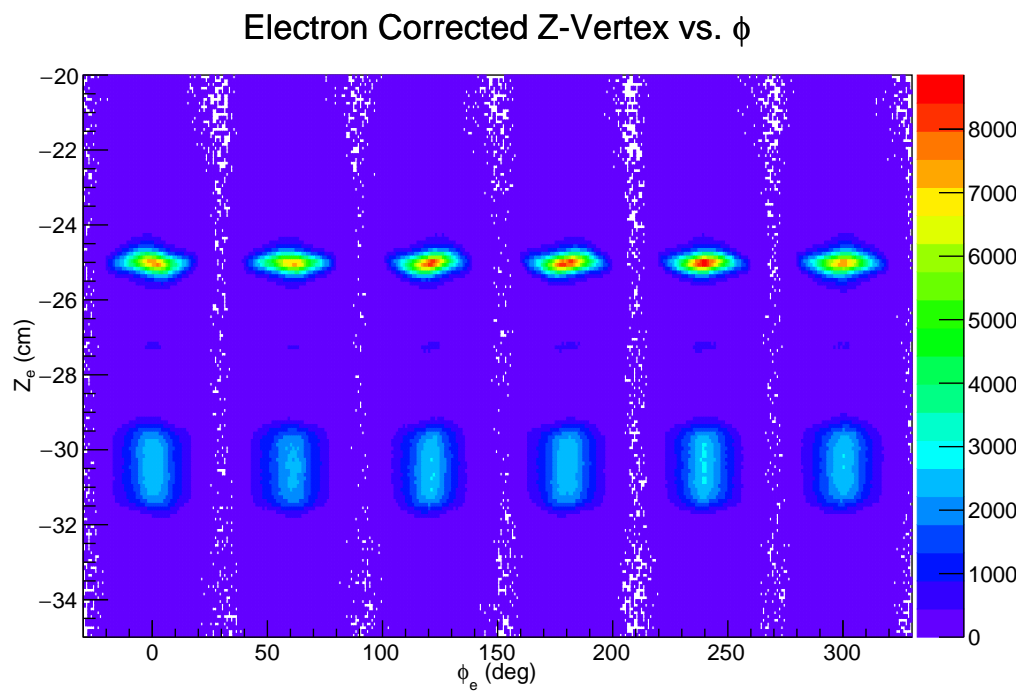
Figure 2.11: Plot of corrected electron vertex vs. azimuthal angle.
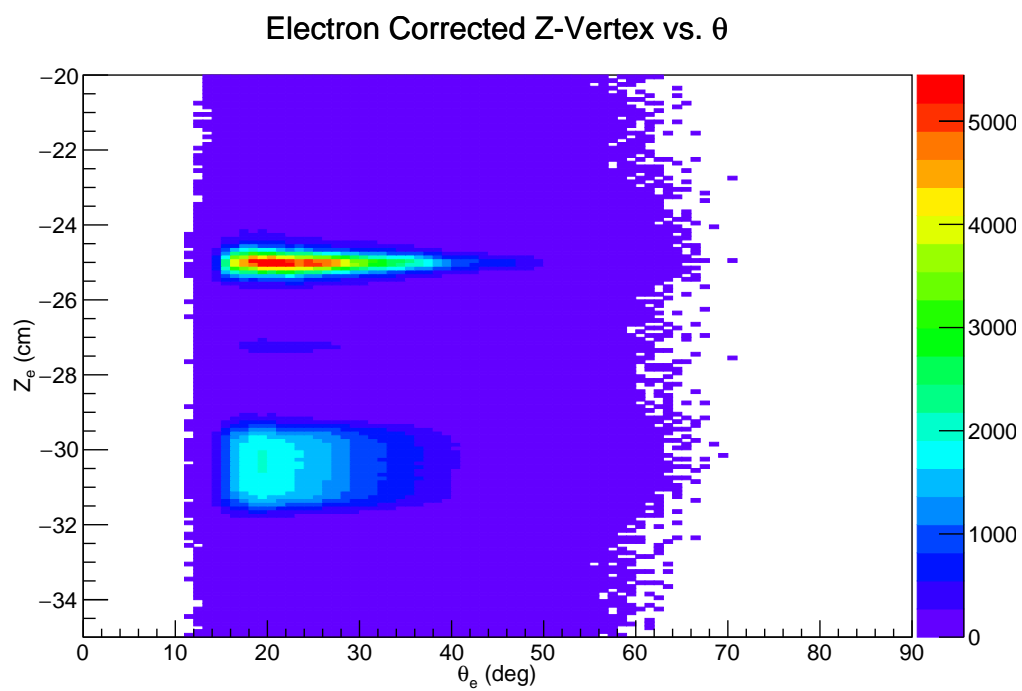
Figure 2.12: Plot of corrected electron vertex vs. polar angle.

2.1.3 Electron Fiducial Cuts

The electron fiducial cut is used to remove events from regions where the detection efficiency and acceptance is rapidly changing. The basic idea is to look for the range of azimuthal angles at a given polar which give a stable electron yield. A continuous parametrization can then be developed.

In this analysis, we use the approved electron fiducial cuts developed for *EG2c* [10, 11]. In figure 2.13a, we plot the scattered electron polar vs. azimuthal angle from the Deuterium target prior to the fiducial cuts; in figure 2.13b, we plot the same quantities after the cuts.

(a) Before fiducial cuts. (b) After fiducial cuts.
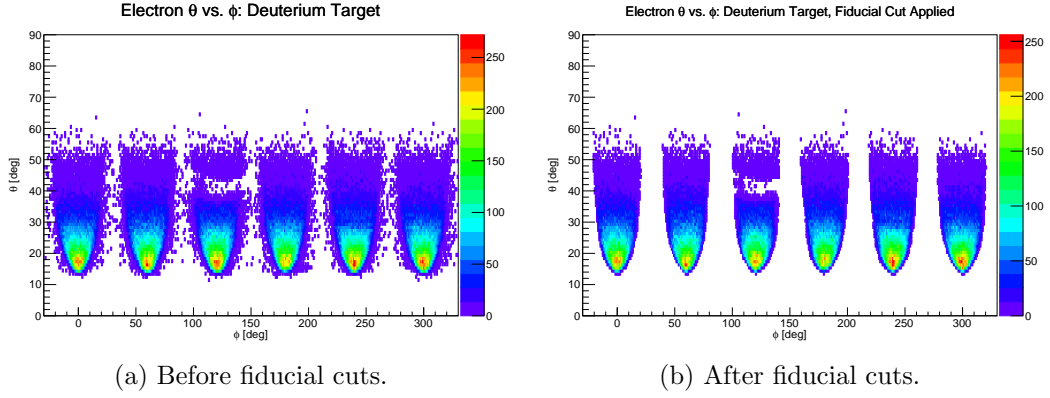
Figure 2.13: Plot of scattered electron θ vs. ϕ for one run on the Deuterium target.

2.2 Proton Selection

2.2.1 Proton Particle Identification

Although this analysis is an inclusive cross-section ratio measurement, we use protons for the kinematic corrections discussed below. So, we have to correctly reconstruct proton events.

The procedure to reconstruct protons is identical to the one used for a prior approved *EG2c* analysis [11]. For positive particles, we can determine the momentum in the drift chamber; for a given momentum, we can calculate the time when a proton should arrive at the hodoscopes. If the particle arrives at the hodoscopes at the calculated time, it is most likely a proton. To quantitatively do this, we create a corrected time-of-flight variable defined as

$$TOF_{corr} = T^P_{SC} - EST - T^P_{Calc} \qquad (2.3)$$

, where T^P_{SC} is the measured time of the proton candidate hitting the hodoscope, EST is the event start time, and T^P_{Calc} is the calculated time-of-flight from the vertex to the hodoscope for a given path-length and momentum for a proton. In figure 2.14 (top), we plot this corrected time-of-flight for all positive particles. The protons should have a corrected time-of-flight equal to zero.

In order to select protons, the data is binned in momentum. For every momentum bin, a Gaussian fit is made and the standard deviation is determined. Then events within $\pm 2\sigma$ are kept, using a continuous parametrization. The cut parameters are taken from the approved *EG2c* analysis [11]. The events remaining after the proton PID cut are shown in figure 2.14 (bottom).

2.2.2 Proton Vertex Corrections

The proton vertex corrections are done in exactly the same way as the electron vertex corrections described above. Figure 2.15 shows the reconstructed proton vertex before the corrections, and figure 2.16 shows the reconstructed proton vertex after the corrections.

When performing the kinematic corrections we don't cut directly on the corrected proton vertex, but rather we cut on the corrected electron vertex and the difference between the corrected electron and proton vertices (figure 2.17).
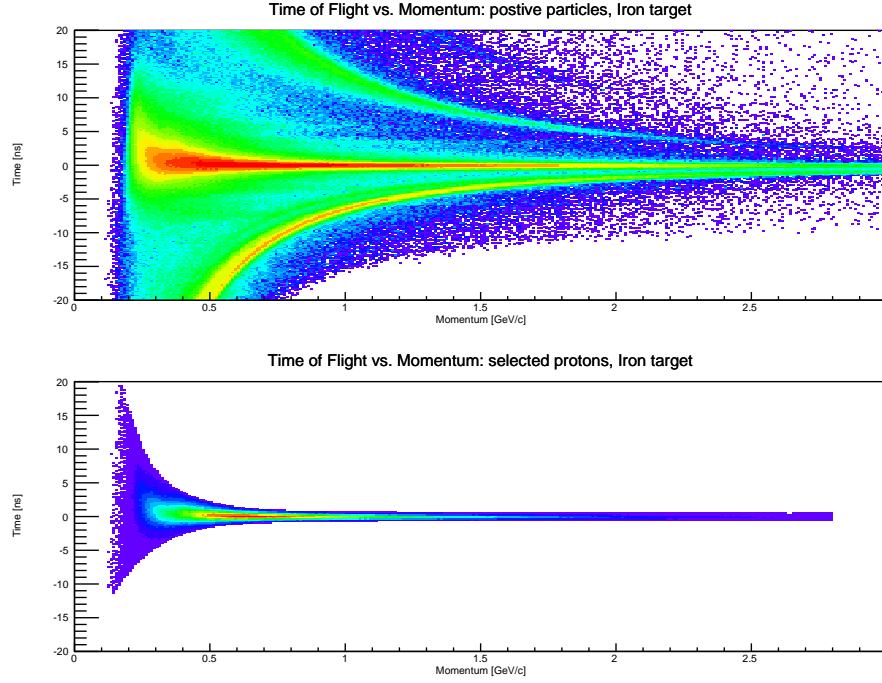
Figure 2.14: Proton PID. Top: Corrected Time-Of-Flight vs. Momentum for positive particles from the Iron target. The Z-axis is in log scale. Bottom: Events that pass the proton PID cuts.

2.2.3 Proton Ionization Energy Loss Corrections

Using the *CLAS* monte-carlo simulation (GSIM), we can calculated the proton ionization energy loss correction. In figure 2.18, we plot the true minus the reconstructed proton energy vs. the reconstructed proton momentum. From this, we develop a continuous parametrization for the energy loss correction as a function of momentum. It was found that the same correction can be used for the liquid deuterium and the liquid hydrogen targets.
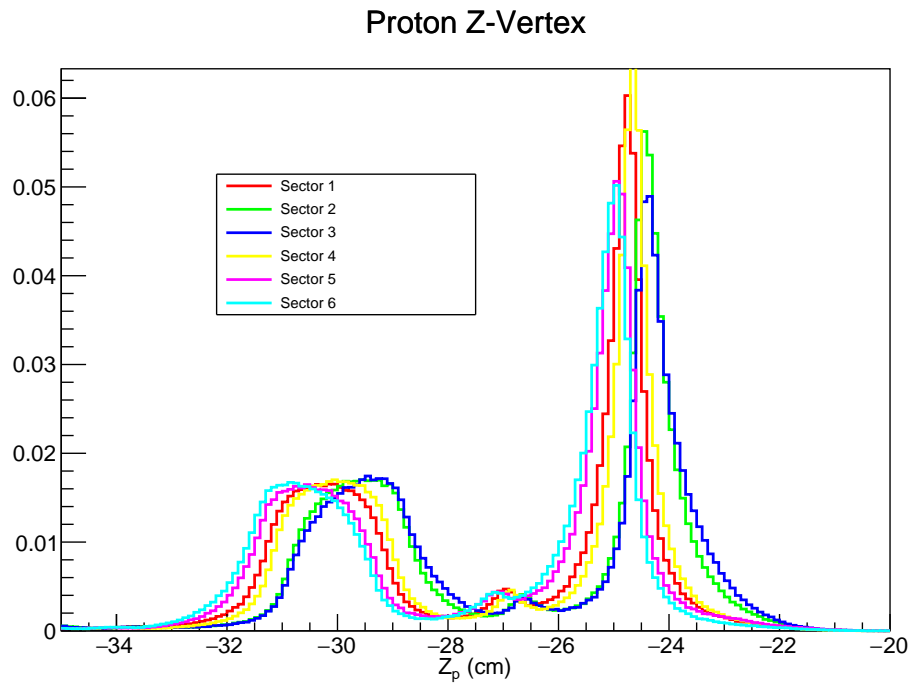
Figure 2.15: Proton reconstructed vertex before vertex corrections for Carbon/Deuterium data.
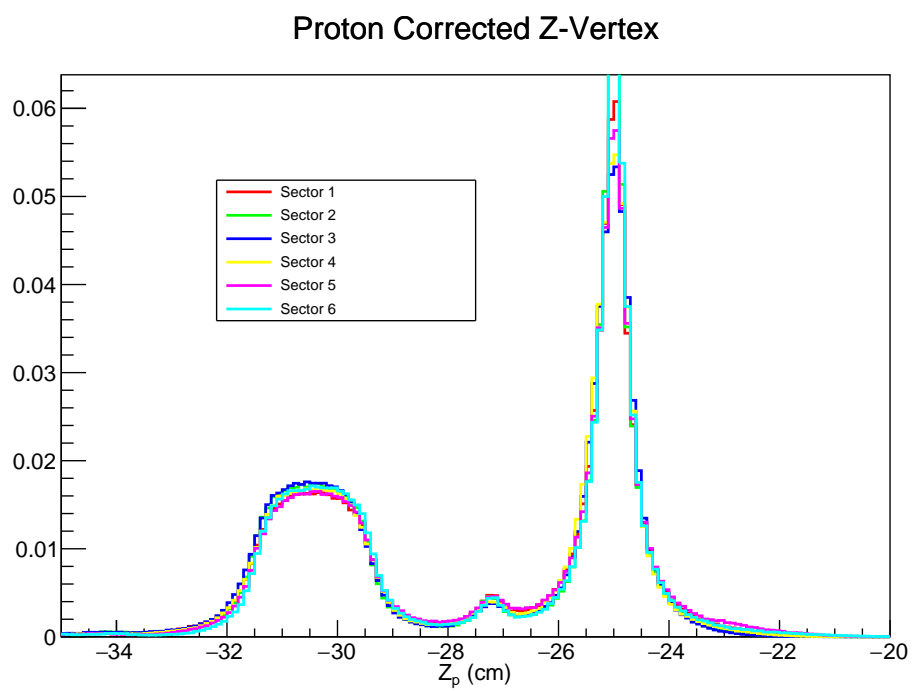
Figure 2.16: Proton reconstructed vertex after vertex corrections .or Carbon/Deuterium data

Figure 2.17: Proton minus electron corrected vertex difference. For the kinematic corrections described below, the vertex difference was required to be less than 2 cm.

Figure 2.18: Proton ionization energy loss corrections as determined by simulation. The parameters in this plot can be used for both the liquid Deuterium and Hydrogen targets.
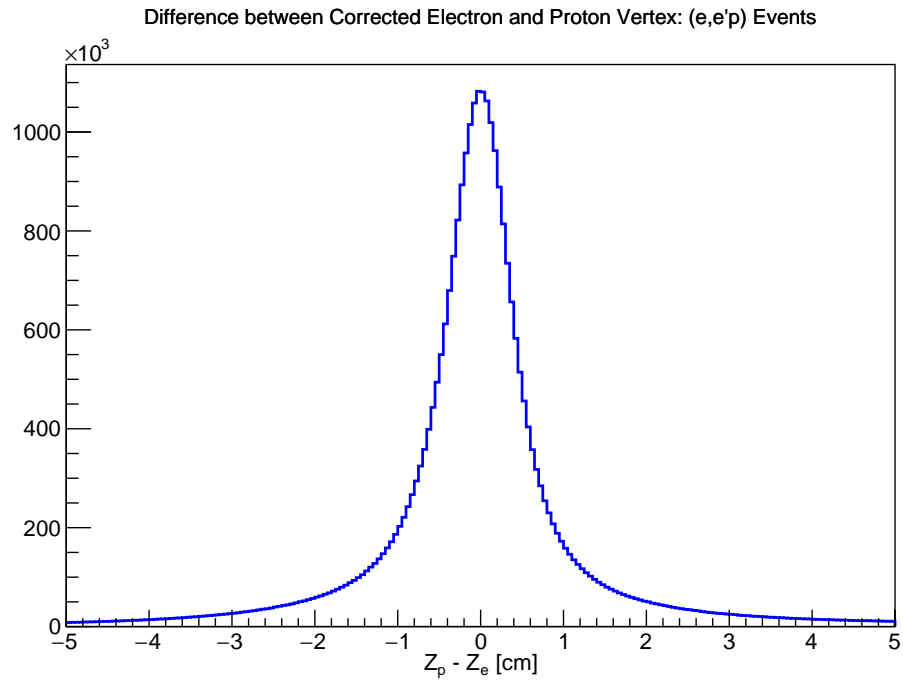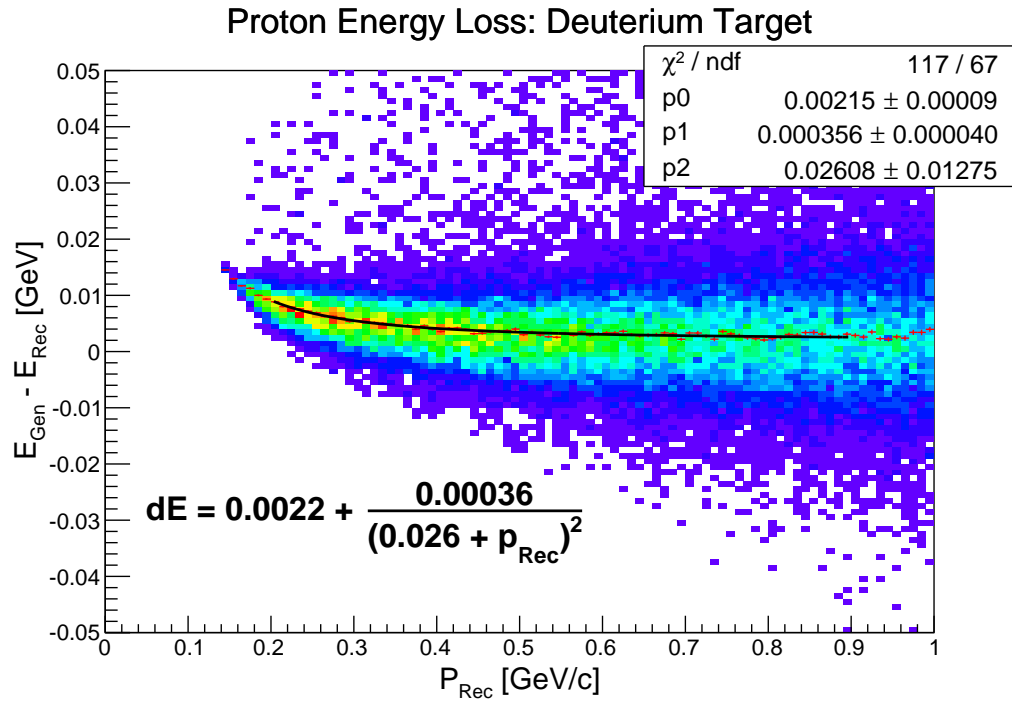
Chapter 3

Kinematic Corrections

There exist several potential imperfections which can cause the incorrect reconstruction of particles' momentum vectors. Incomplete knowledge of the torus magnetic field distribution will affect the reconstruction of the momentum. Misalignment of the drift chambers, wire sag, limited knowledge of wire feed-through locations, etc. can affect both the reconstructed angles and momentum. The originally developed empirical momentum corrections assumed the angles to be reconstructed correctly and used e-p elastic scattering to correct the electron momentum [13]. After additional studies [14] found that the angles may not be reconstructed perfectly, more complex correction schemes were developed incorporating all the effects described above [15, 16].

Here we first correct the beam energy using information obtained from the Hall A arc. Then we correct the electron and proton polar angles using e-p elastic scattering, based on the technique using in reference [17]. For DIS events, we use radiative elastic events from the Hydrogen target to correct the magnitude of the electron momentum [18]. Finally, for QE events, we estimate the magnitude of the momentum correction by using the Deuterium target. No fiducial cuts are applied in this chapter so that the fits can cover a larger range.

3.1   Electron Beam Energy

For the *EG2c* run period, the set electron beam energy was 5.014 GeV. However, it is known that the set energy during 6 GeV *CEBAF* running

was not equal to the true energy [19]. Since Hall A was in operation during the same time, the beam energy can be determined using the Hall A arc measurements. Hall A ran at both 2nd pass and 4th pass during this time. They measured the following beam energies:

$$Injector + 4 \times Accelerator = 4019.5 MeV \, (Hall A \, 4^{th} \, Pass)$$

$$Injector + 2 \times Accelerator = 2039.7 MeV \, (Hall A \, 2^{nd} \, Pass)$$

From this, we can determine what the beam energy in Hall B (operated at 5th pass) should be. We calculate the following beam energy:

$$EG2c \, Energy = 5009.4 \, MeV$$

This is the beam energy we use for the remainder of this analysis. As can be seen if figure 3.1, for H(e,e') events, using this energy brings the elastic peak closer to the proton mass.

3.2 Scattering Angle Corrections

To correct the reconstructed polar angles, we apply a procedure similar to that done in reference [17]. We first select events from the Hydrogen target where the scattered electron and one proton were detected. We take events where the invariant mass, W, reconstructs to within the elastic peak (figure 3.2a). Then we require the detected electron and proton to be coplanar (figure 3.2b). With these two cuts, we select elastic scattering events with potentially some soft photon radiation.

Next, for elastic scattering, we can calculate the beam energy using the electron and proton angles only [14] as

$$E_0 = \frac{M_p}{1 - \cos \theta_e} \left(\cos \theta_e + \frac{\sin \theta_e}{\tan \theta_p} - 1 \right) , \tag{3.1}$$

where M_p is the mass of the proton and θ_e and θ_p are the angles of the electron and proton, respectively. This is the important point - the reconstruction of the beam energy is done solely from the two angles, so any mis-reconstruction of the beam energy will have to be because of angular mis-reconstruction. In figures 3.3 and 3.4, we show the ratios of the true energy to the energy reconstructed from the angles.
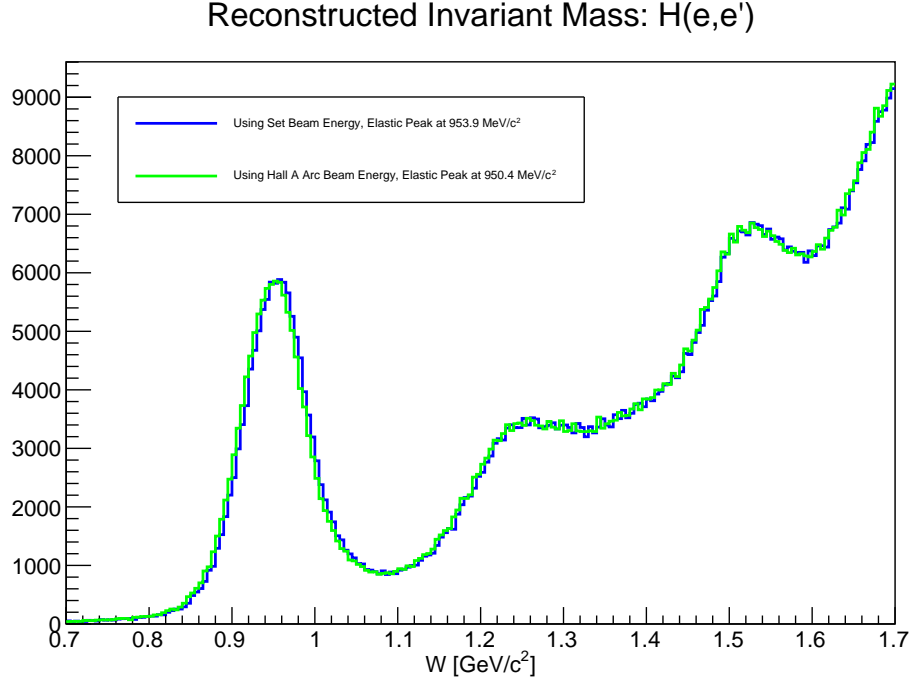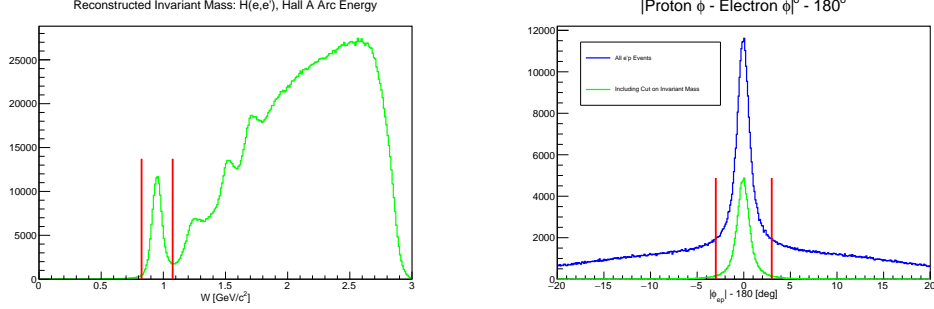
Figure 3.1: Reconstructed invariant mass for H(e,e') events using the two different beam energies.

Under certain reasonable assumptions [17], the mis-reconstruction should be the same for all types of particles. So, for every event, we can find the distance of closest approach to the electron-proton angle dependency curve for the true energy (figure 3.5). This will give us two angle correction values for every event, one for the electron and one for the proton. Since we assume the form of the correction is the same for both types of particles, the angles lose their individual identities here, and we roll both into a general polar angle for doing the correction.

In figure 3.6, we show the difference between the measured and calculated general polar angle vs. the measured general polar angle. Note how there are two groups of data in this plot, the lower angles coming from the electron and the larger angles coming from the proton. For every sector, we look at the difference between the calculated and measured general polar angles vs. ϕ (figure 3.7a), and we fit the difference with a $3^r d$ order polynomial. After applying this correction to both the electron and proton reconstructed angles,

(a) Reconstructed invariant mass for H(e,e'p) events, and the selection of the elastic peak (within red lines).

(b) Difference between the absolute value of the electron and proton azimuthal angles minus 180 degrees. We select events between the red lines.

Figure 3.2: Elastic selection cuts.

we see no dependence on ϕ (figure 3.7b). We checked for any dependence on θ (figure 3.8), and saw very little; so, we made the correction only a function of ϕ. In figures 3.9a and 3.9b, we show the reconstructed energy using the corrected angles.

The correction should be valid for all types of particles. Since we see very little dependence of the correction on θ, it may also be valid for all polar angles. Since we have events with polar angles between 12 and 55 degrees in the fit, we can at least say that the fit is valid in that range. For this inclusive (e,e') analysis, the scattered electron is never outside this range.

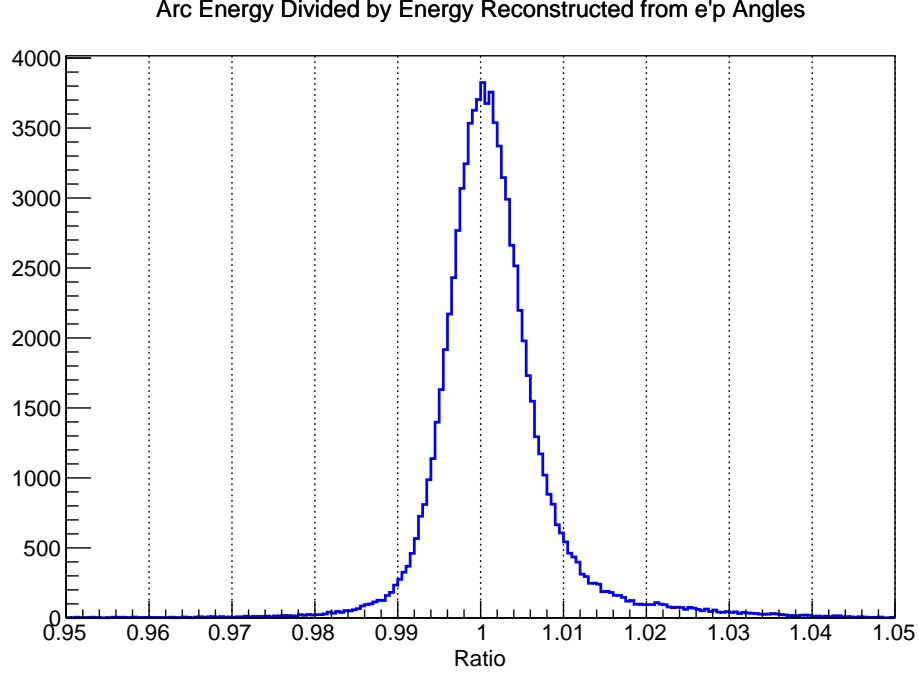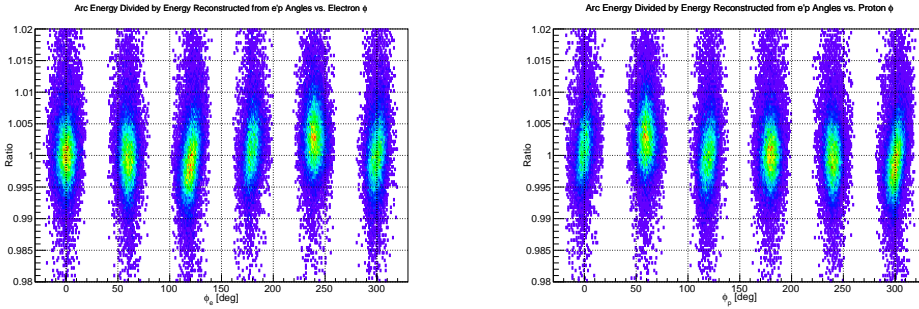Figure 3.3: True beam energy divided by the energy determined from the electron and proton polar angles.

(a) True beam energy divided by the energy determined from the electron and proton polar angles vs. the electron azimuthal angle.

(b) True beam energy divided by the energy determined from the electron and proton polar angles vs. the proton azimuthal angle.

Figure 3.4: Beam energy reconstructed from angles.
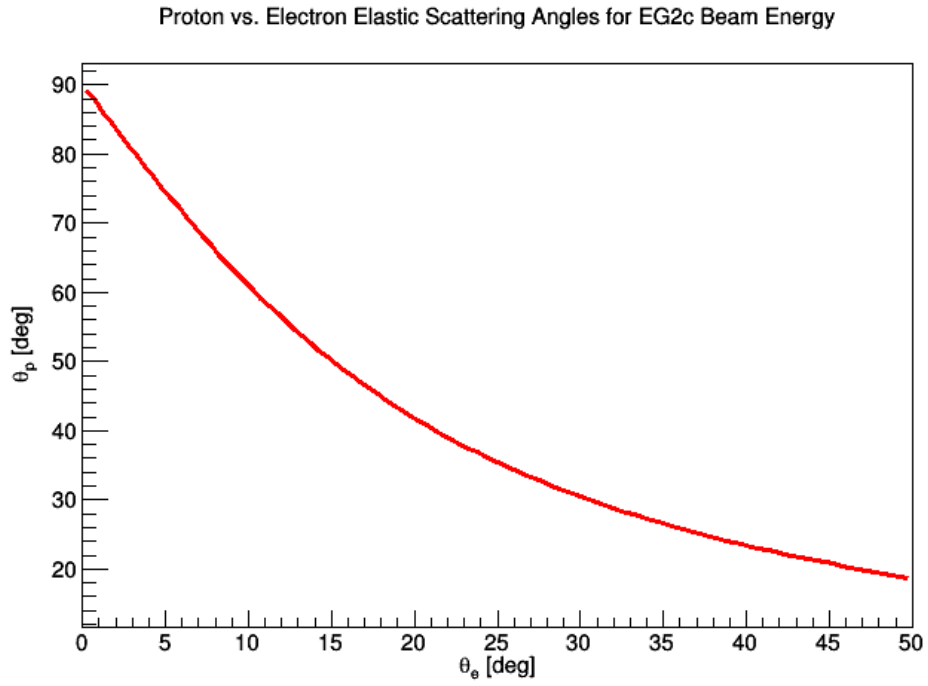
Figure 3.5: Relationship between proton and electron scattering angles for elastic e-p scattering at the true *EG2c* beam energy (equation 3.1). Every selected e-p event, will lie off this curve. By determining the point of closest approach, we can determine a correction to both the electron and proton angles for each event.
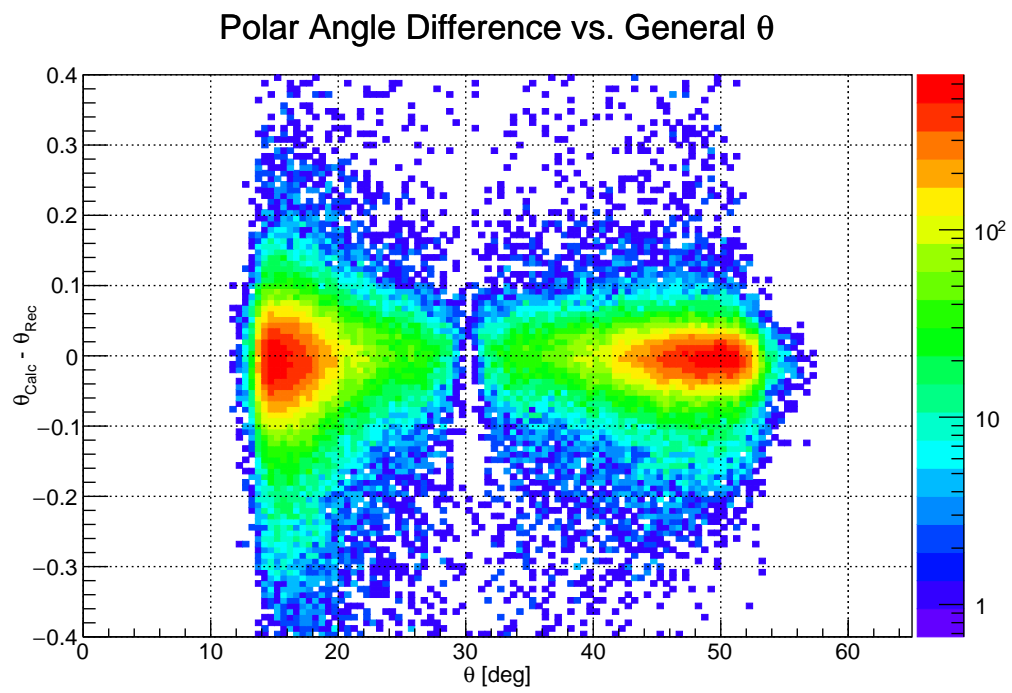
Figure 3.6: The difference between the measured and calculated general polar angle vs. the general polar angle.

(a) Before Corrections

(b) After Corrections.

Figure 3.7: The difference between the measured and calculated general polar angle vs. the general azimuthal angle. We fit each sector with a 3rd order polynomial. The top plot shows before applying any corrections; the bottom after applying the determined correction to both the electron and proton angles.

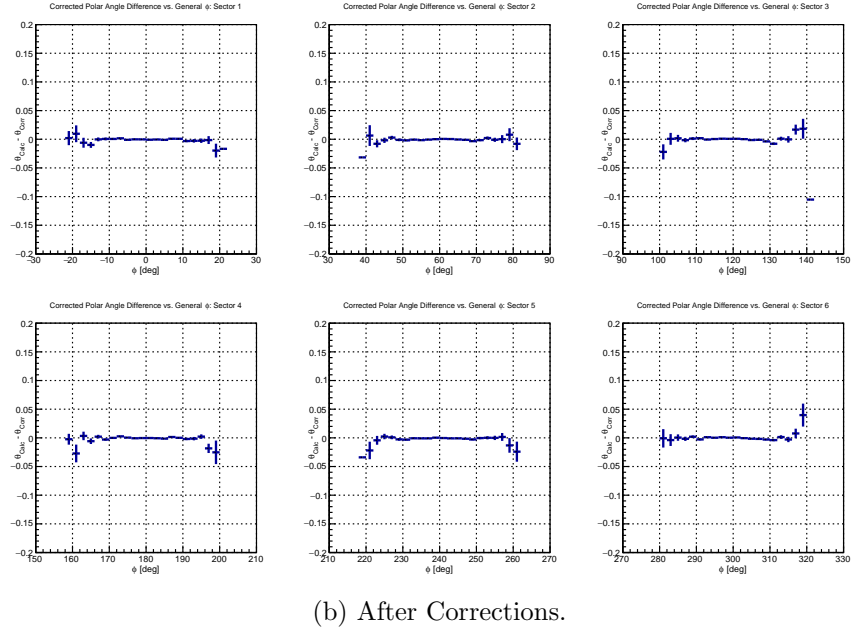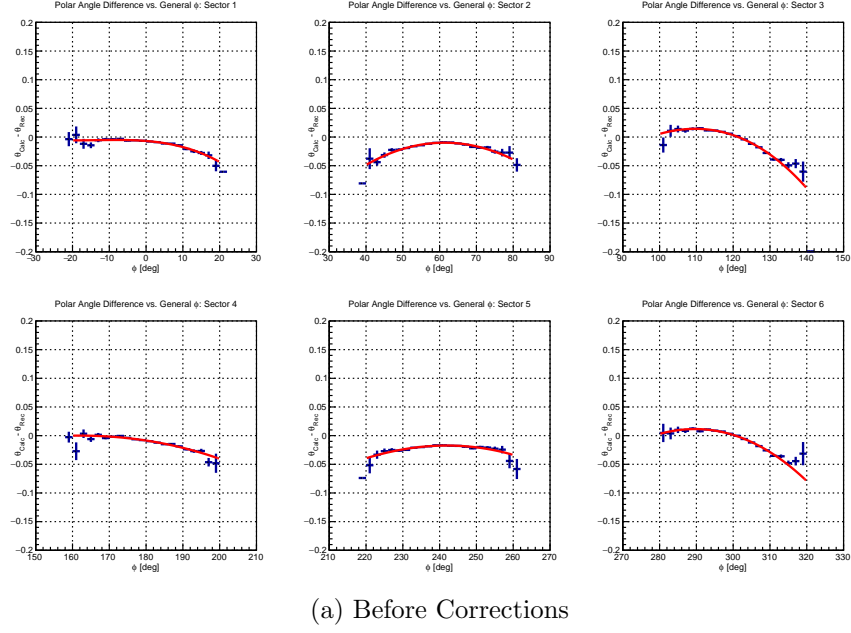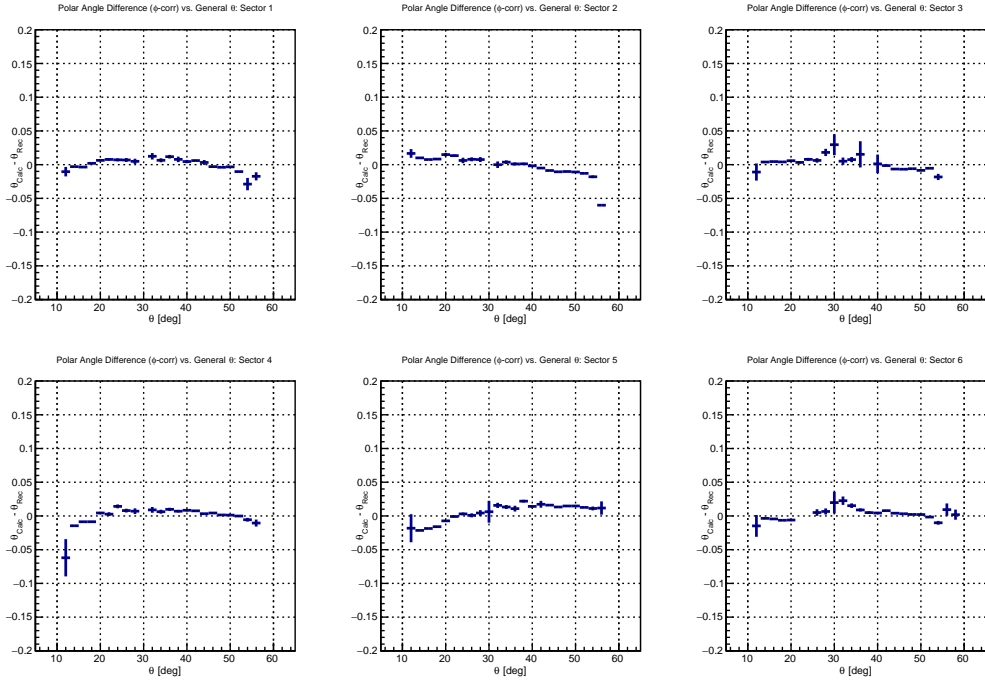Figure 3.8: The difference between the measured and calculated general polar angle vs. the general azimuthal angle after applying the azimuthal determined correction to both the electron and proton events. Since we see very little dependence on the polar angle, we don't make any fit here.
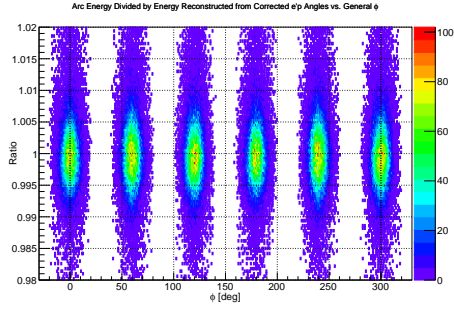
(a) True beam energy divided by the energy determined from the electron and proton polar angles vs. the general azimuthal angle after applying the polar angle corrections.
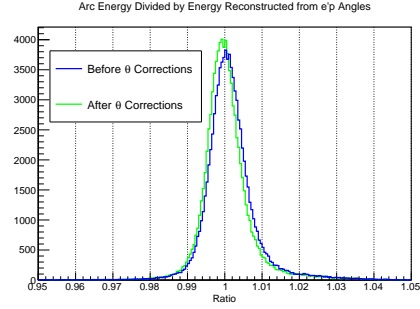
(b) Comparison of true beam energy divided by the energy determined from the electron and proton polar angles before and after applying the polar angle corrections.

Figure 3.9: Beam energy reconstructed from angles after corrections.

3.3 Momentum Corrections

3.3.1 Momentum Corrections for DIS Events

Now that we have corrected the polar angles, we can use these corrected electron and proton angles to calculate any quantity for elastic scattering. Part of our analysis, however, takes place in the inelastic region. As is well known, many of the events in the large invariant mass region come from the so-called radiative elastic tail [20]. If we can select H(e,e'p)X events where the electron reconstructs as a DIS event, but in reality is an elastic event where the incoming electron radiated a hard photon, we can calculate what the true electron momentum should be as

$$E_f = \frac{E_i}{1 + E_i(1 - \cos\theta_e)/M_p} \, , \tag{3.2}$$

where E_f is final electron energy, and E_i is the initial electron energy. Note that E_i is not equal to the beam energy here since the initial electron must radiate prior to the elastic scattering to perform the correction, and it must be calculated from equation 3.1.

To select the required events, we first look at the reconstructed missing mass when we detect and electron and proton for different invariant mass regions. As can be seen in figure 3.10, the resolution is degraded at large invariant mass. So to select radiative elastic events where the initial electron radiated, we first require the electron and the proton to be coplanar (figure 3.11). From this plot, we estimate the inelastic contribution under the cut peak to be $\approx$ 8-10%. In order to reduce this background, and remove events where the scattered electron radiated, we require the missing momentum to be along the direction of the beam-line (figure 3.12). Now, assuming elastic scattering (after radiation), we calculate the initial electron momentum and compare that to the sum of the scattered electron and proton momentum along the beam-line (figure 3.13). We require this difference to be less than 100 MeV/c.

Now that we've selected the events, we consider the missing momentum vs. the invariant mass (figure 3.14a). For the events passing all our cuts, we clearly see the radiative rail rising at high invariant mass. Then in figure 3.14b, we plot the scattered electron momentum vs. polar angle for the radiative elastic events with large invariant mass. We can see that these events cover the same area of phase-space as the inelastic events.
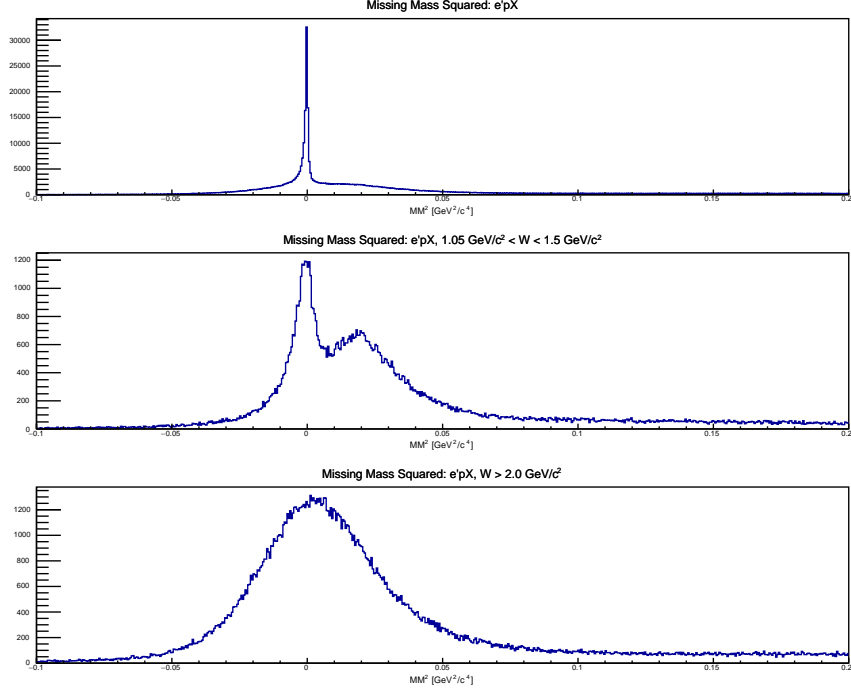
Figure 3.10: Square of the missing mass for H(e,e'p)X events. Top: All events. Middle: Events with invariant mass near the 3-3 resonance. Bottom: Events with large invariant mass.

For every event, we calculate the scattered electron momentum from the measured (corrected) electron and proton angles [18]. We then define the following correction functions:

$$\frac{P_{e,calc}}{P_{e,meas}} = f(\phi) \times g(\theta)\,, \tag{3.3}$$

where $f(\phi)$ and $g(\theta)$ are once again 3rd order polynomials; and the justification for this factorization comes from previous momentum-correction studies [13]. In each sector, we bin the data in ϕ and determine $f(\phi)$ (figure 3.15a). Then we divide equation 3.3 by $f(\phi)$ and bin the data in θ to determine $g(\theta)$ (figure 3.15b). After applying the correction, we remove the dependence on ϕ and θ (figures 3.16a and 3.16b). We compare the square of the missing mass before and after the momentum corrections in figure 3.17.

The last question we considered was whether these corrections could be used for the solid targets, located several centimeters downstream of the
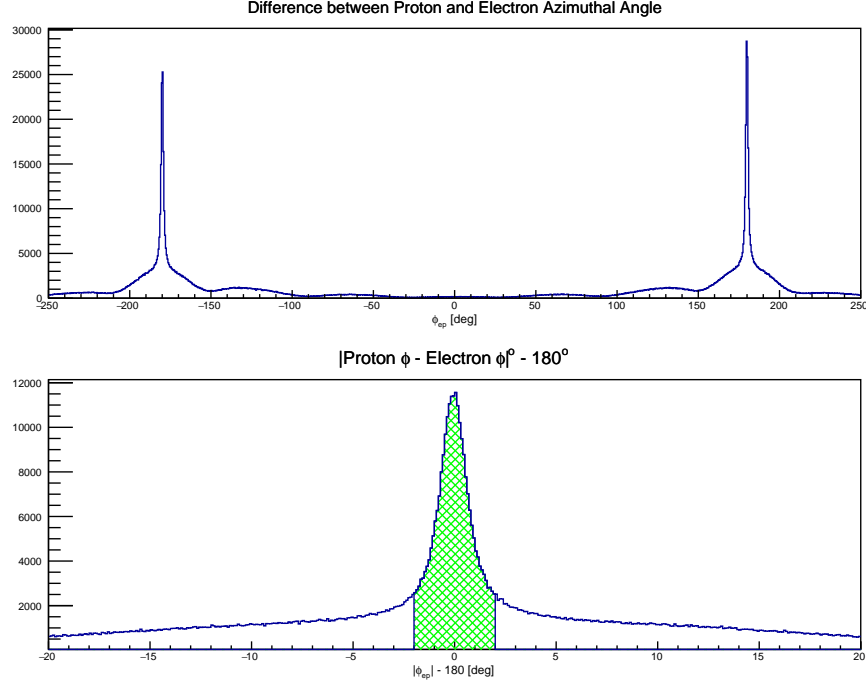
Figure 3.11: Top:Difference between the proton and electron azimuthal angles. Bottom: Absolute value of the difference between the electron and proton azimuthal angles minus 180 degrees. We select events with this quantity $< \pm 2^o$. The background under the peak was estimated and reduced by additional cuts.

cryo-target. First note how in figure 3.15a, the ratio was primarily above unity. This is because no ionization energy loss corrections had been applied for the electron. This correction is rolled into the momentum correction. By using *GSIM*, we were able to determine that the electron ionization energy loss is identical in all the solid and liquid targets. So, there is no issue with correcting for this in the momentum correction. Next, we binned the hydrogen target as shown in figure 3.18, and looked at the correction for the two regions. In figures 3.19a and 3.19b, we see that the corrections look qualitatively similar for the two bins, even though the bin centers differ by about 2 cm. This provides some justification for using the obtained correction factors for the solid targets.
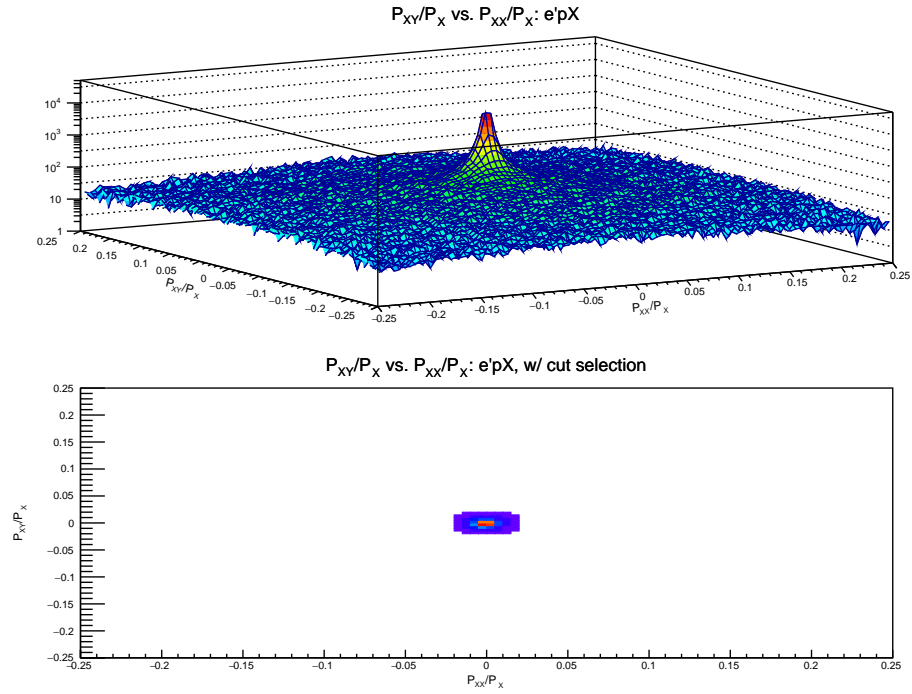
Figure 3.12: Fraction of the missing momentum in the directions transverse to the beam-line. Top: All H(e,e'p)X events. Bottom: Applied Cut on missing momentum direction. Less than 2% of the missing momentum is allowed to be in a direction transverse to the beam-line.

Figure 3.13: Difference between reconstructed initial electron momentum from electron and proton angles and sum of the scattered electron and proton momentum along the beam-line. The absolute value of this difference is required to be less than 100 MeV/c.

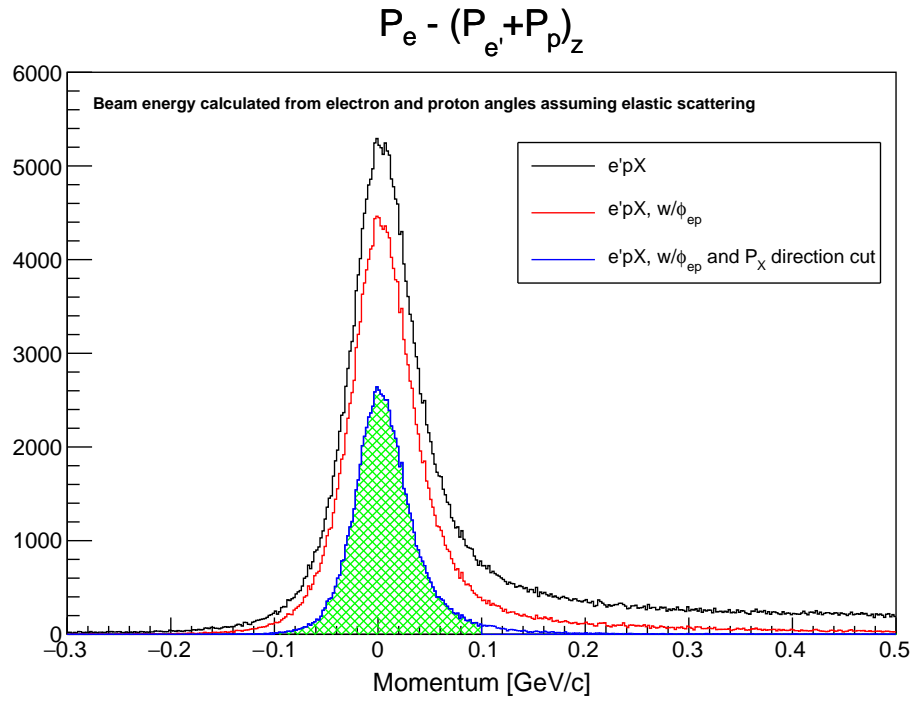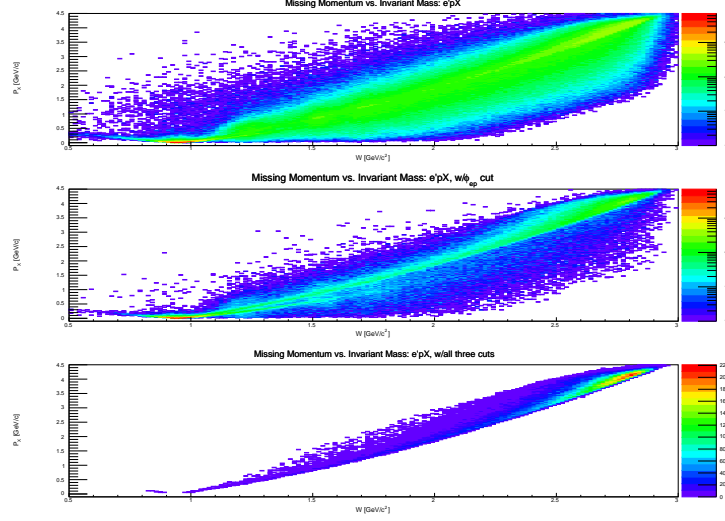(a) Missing momentum vs. invariant mass. Top: All H(e,e'p)X events. Middle: Events passing the electron-proton co-planarity cut. Bottom: Events passing all three cuts discussed above.
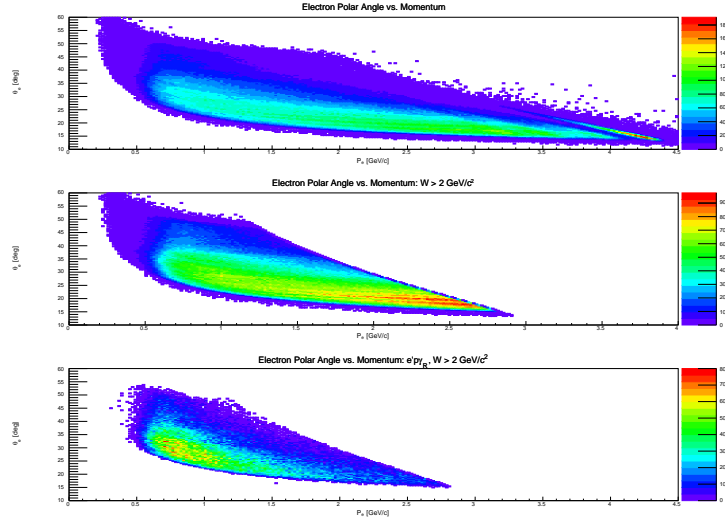
(b) Scattered Electron Momentum vs. Polar angle. Top: All H(e,e') events. Middle: H(e,e') events, with invariant mass > 2 GeV. Bottom: Radiative Elastic $H(e, e'p)\gamma$ events, with invariant mass > 2 GeV.

Figure 3.14: Event distributions after radiative elastic event selection.
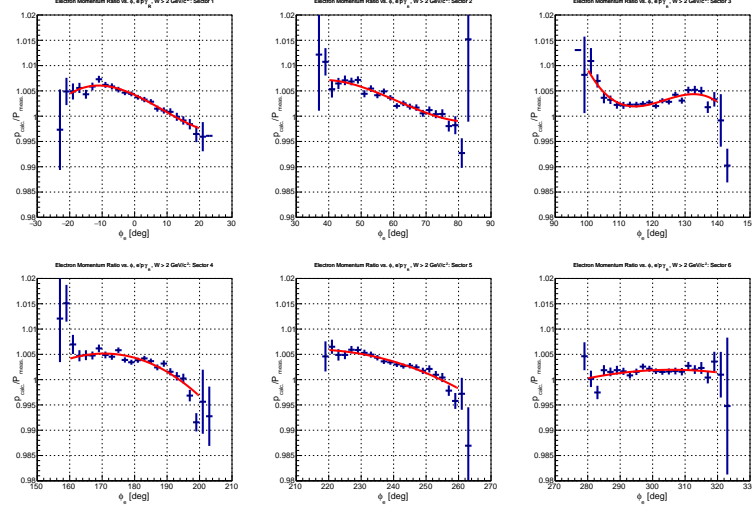
40

(a) Ratio of calculated to measured electron momentum vs. ϕ for radiative elastic events. The ratios are fit with a 3rd degree polynomial to determine $f(\phi)$.
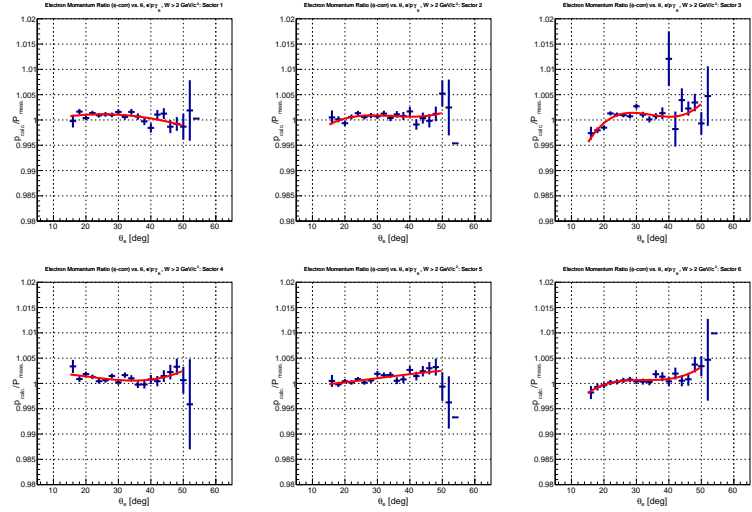
(b) Ratio of calculated to measured electron momentum divided by $f(\phi)$ vs. θ for radiative elastic events. The ratios are fit with a 3rd degree polynomial to determine $g(\theta)$.

Figure 3.15: Electron momentum correction ratios before applying corrections.
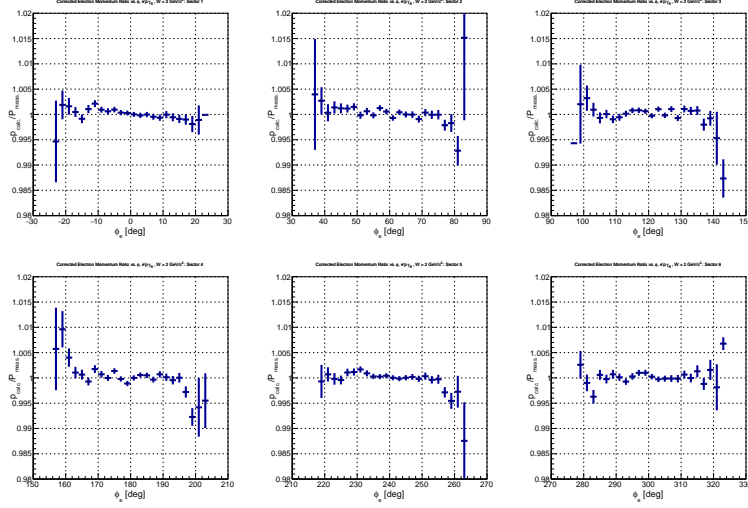
(a) Ratio of calculated to measured electron momentum vs. ϕ for radiative elastic events after applying the electron momentum corrections.
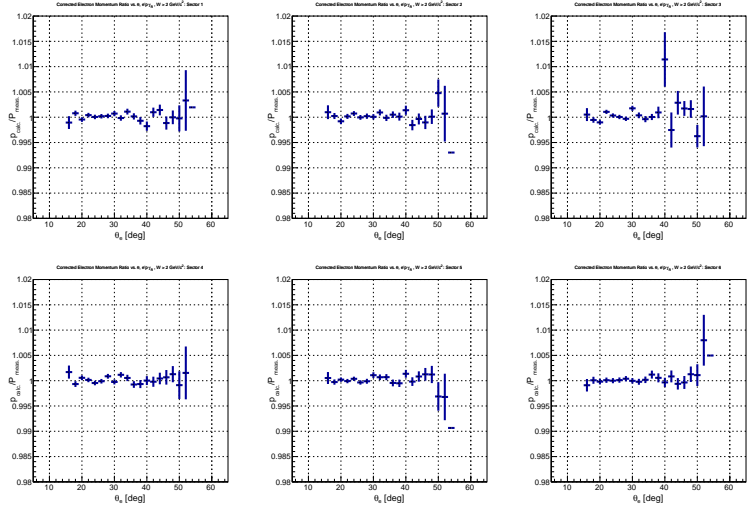
(b) Ratio of calculated to measured electron momentum vs. θ for radiative elastic events after applying the electron momentum corrections.

Figure 3.16: Electron momentum correction ratios after applying corrections.
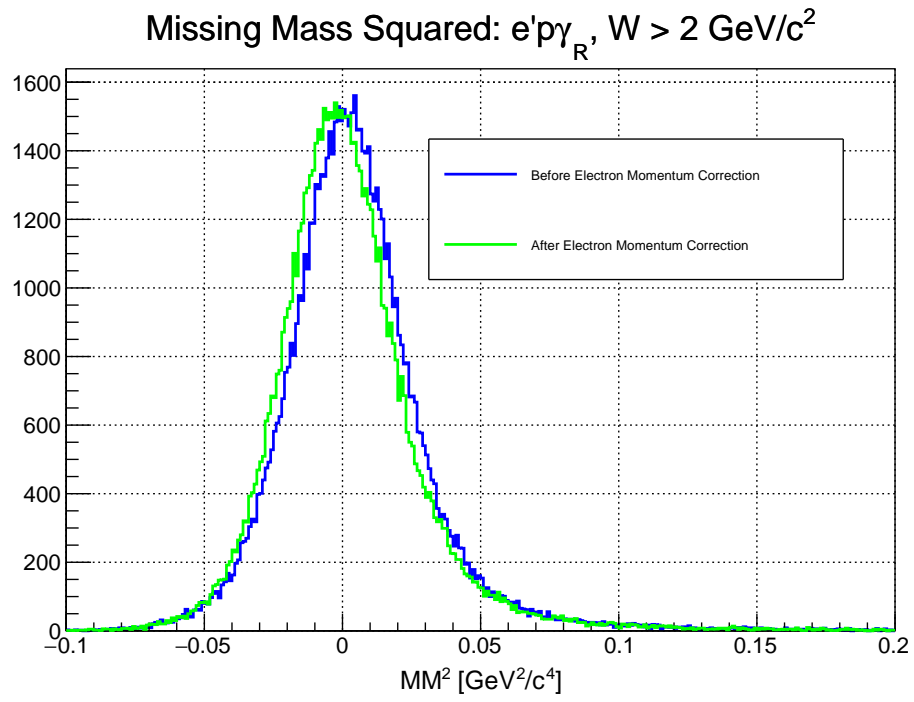
Figure 3.17: Comparison of the square of the missing mass for radiative elastic events before and after applying the electron momentum corrections.
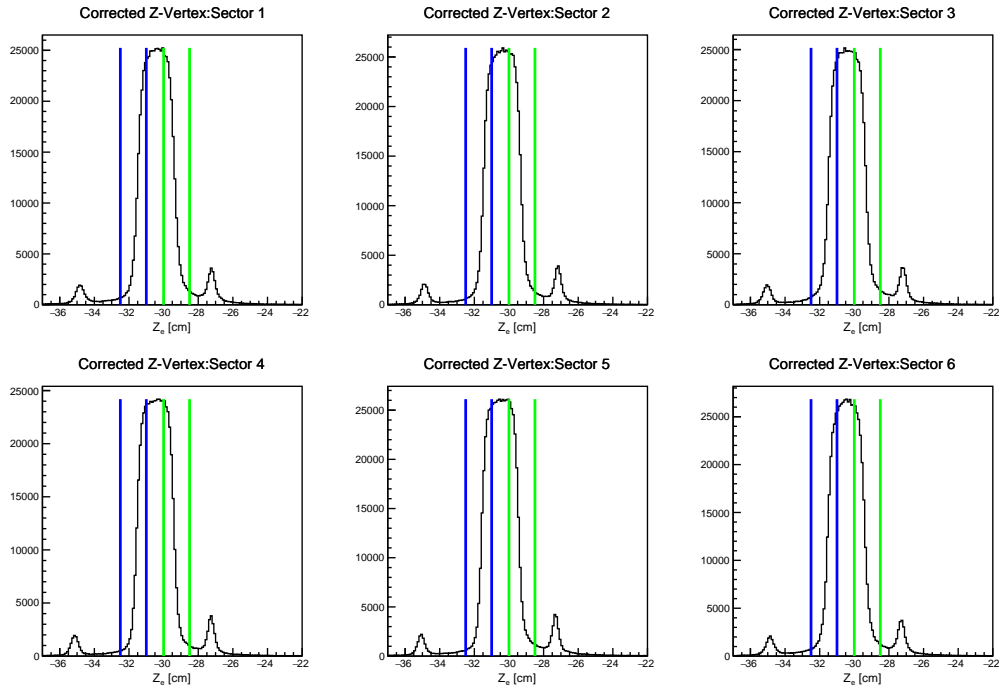
Figure 3.18: Corrected reconstructed electron Hydrogen target vertex for the six sectors. We study the momentum corrections for two different regions of the target.
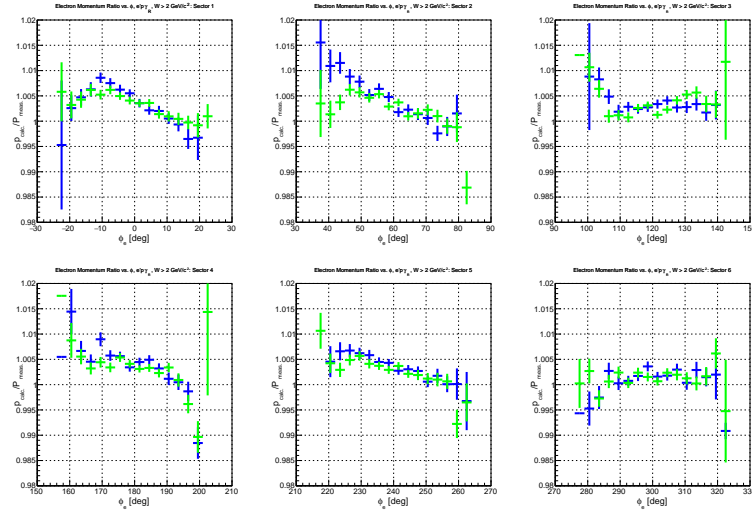
44

(a) Ratio of calculated to measured electron momentum vs. ϕ for radiative elastic events with large invariant mass. The data is shown for the two regions of the Hydrogen target selected in figure 3.18.
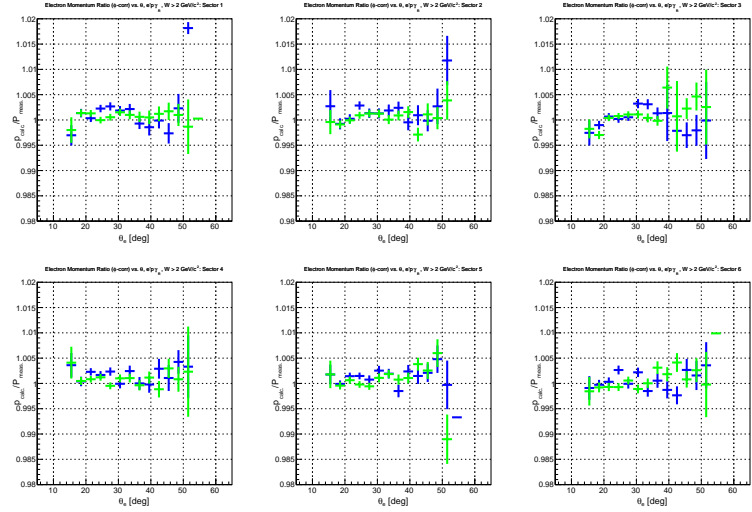
(b) Ratio of calculated to measured electron momentum vs. θ for radiative elastic events with large invariant mass. The data is shown for the two regions of the Hydrogen target selected in figure 3.18.

Figure 3.19: Electron momentum correction ratios for different Hydrogen target regions.

45

3.3.2   Momentum Corrections for QE Events

For our QE events at large Bjorken-X, the Hydrogen data obviously does not extend into that part of the phase-space. If we consider Deuterium data, we can plot the missing mass for D(e,e'p)X events. As can be seen in figure 3.20 for large Bjorken-X events, there is a clear peak at the nucleon mass. We select the events in the peak. Then assuming that the electron angles, proton angles, and proton momentum are reconstructed correctly, we can calculate the electron momentum [21, 22]. In figure 3.21, we plot the reconstructed and calculated electron momentum. In figure 3.22, we plot the difference between the calculate and measured electron momentum vs. the azimuthal angle; we see that at most the electron momentum is incorrectly reconstructed by 20 MeV/c.

Assuming a 4 GeV/c scattered electron, a 20 MeV/c mis-reconstruction will cause a shift of 0.025 in Bjorken-X at Bjorken-X equal to 1. At Bjorken-X equal to 1.5, this will cause a shift of 0.037. This mis-reconstruction of Bjorken-X can have a small effect on our final ratios, and will be taken into account in the systematic uncertainties.
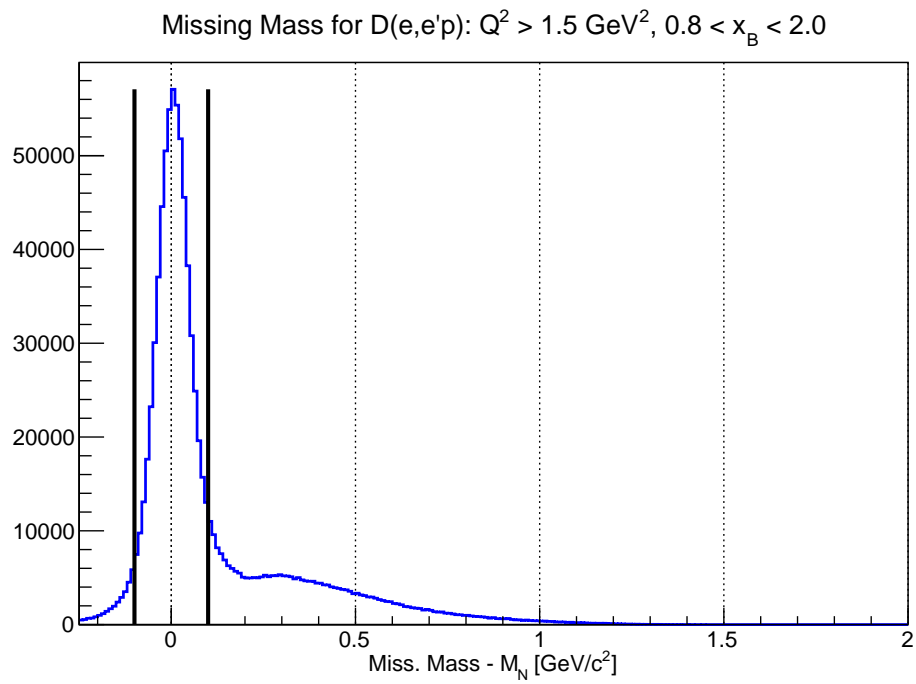
Figure 3.20: Reconstructed missing mass minus the nucleon mass for D(e,e'p)X large Q^2 and Bjorken-X events. We select QE events using the cut shown in the plot.
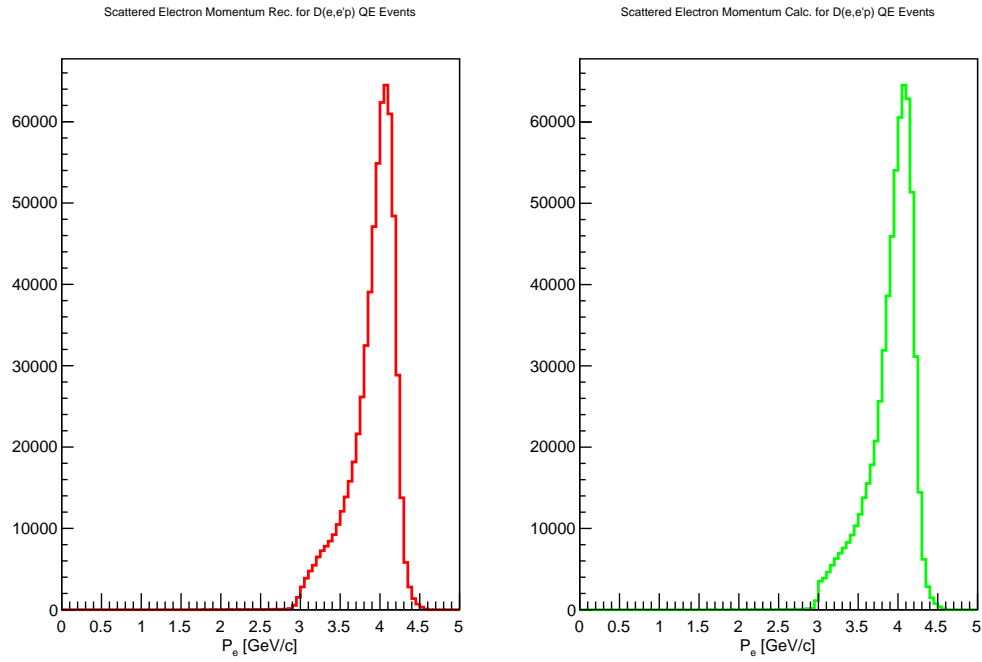
Figure 3.21: Left: Reconstructed electron momentum for D(e,e'p) QE events. Right: Calculated electron momentum for D(e,e'p) QE events, assuming the electron angles, proton angles, and proton momentum are correctly reconstructed.
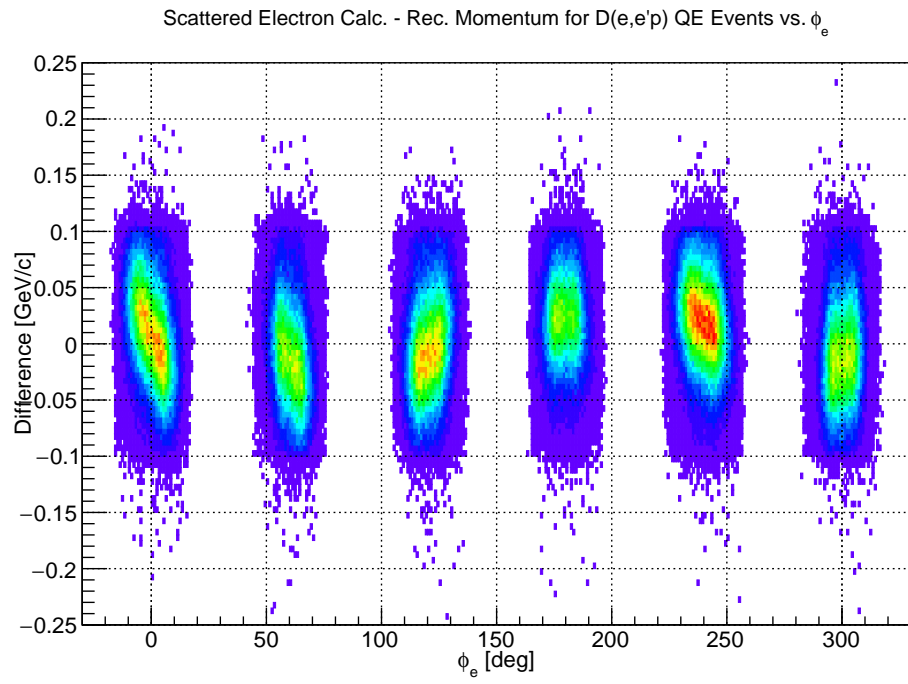
Figure 3.22: Difference between the electron calculated and reconstructed momentum for D(e,e'p) QE events vs. the electron azimuthal angle.

Chapter 4

Data Quality and Background Removal

4.1 Data Quality

In this analysis, we combined all the Deuterium data when calculating the cross-section ratios. In order to select the set of good runs, we looked at the yield for every run corrected for the beam charge and live-time. This follows the procedure of the approved *EG2c* analysis [10]. In figure 4.1, we show the normalized inclusive yield for the Deuterium data. In figures 4.2 and 4.3, we show the normalized inclusive yields for the solid targets. We remove runs which have a larger than 4% deviation from their target's weighted average yield.
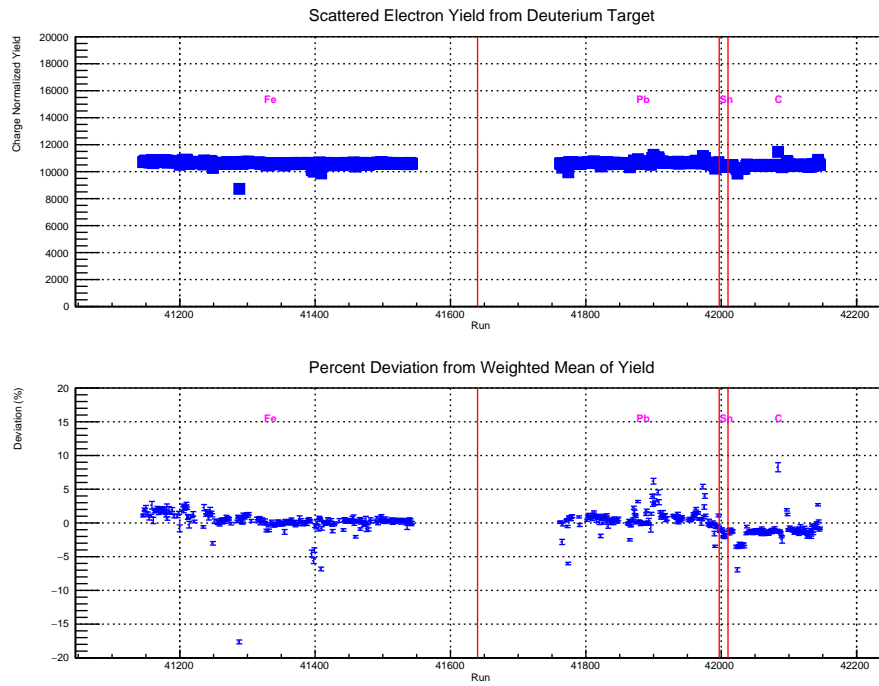
Figure 4.1: Top: Charge normalized yield from the Deuterium target for (e,e') events vs. run number. Bottom: Percent deviation from the weighted average yield vs. run number. In both plots, the vertical red lines demarcate the beginning or ending or a given solid target run period.
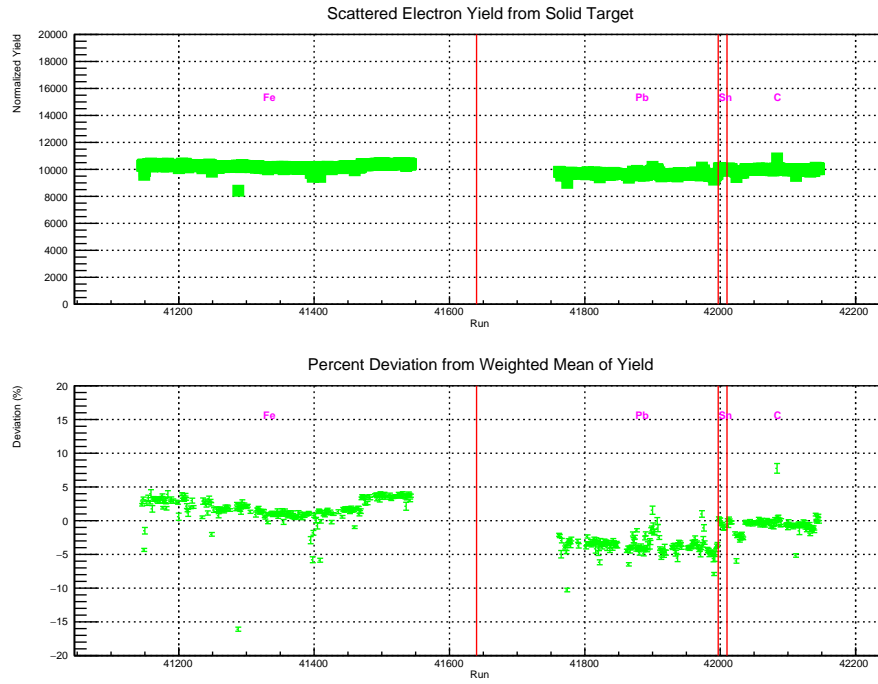
Figure 4.2: Top: Charge and target thickness normalized yield from the four solid targets run concurrently with Deuterium for (e,e') events vs. run number. Bottom: Percent deviation from the weighted average yield vs. run number. In both plots, the vertical red lines demarcate the beginning or ending or a given solid target run period.
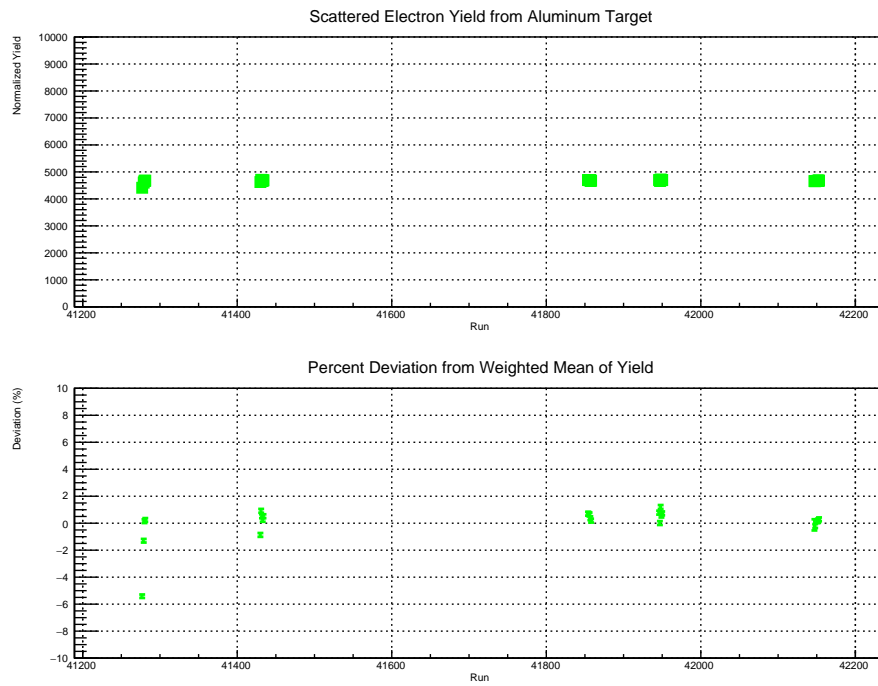
Figure 4.3: Top: Charge normalized yield for the thick Aluminum target vs. run number. Bottom: Percent deviation from the weighted average yield vs. run number.

4.2   Background Removal

In figure 4.4, we show the electron reconstructed vertex for the entire data-set. (The Tin target was found to be shifted by about 1 cm from the other solid targets. It is believed that this may be due to the Tin target not being fully inserted into the beam-line. For this reason, we do not analyse the tin data in this report.)

Corrected Electron Vertex
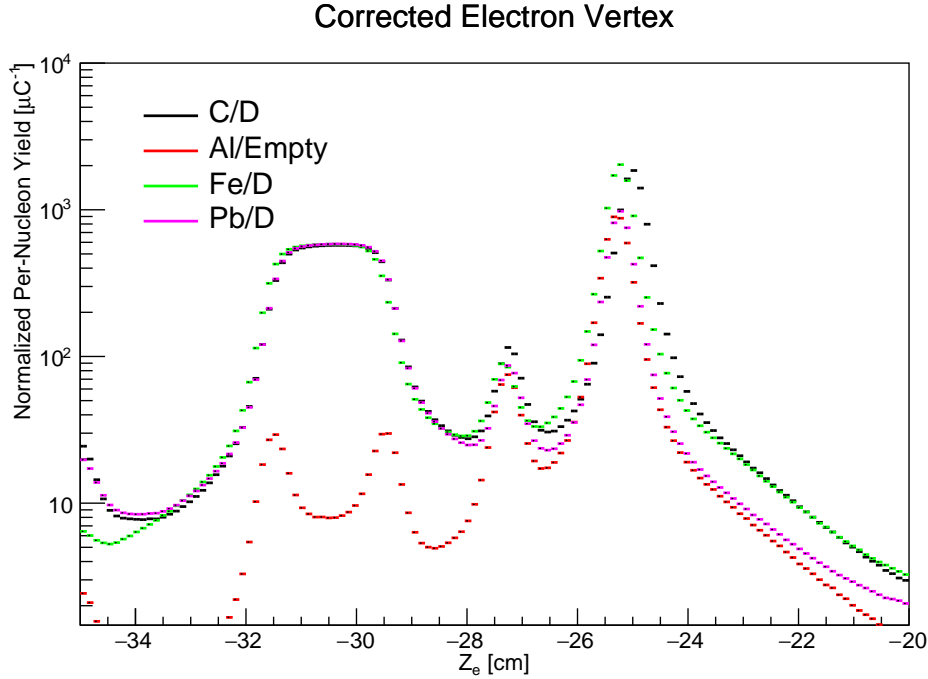
Figure 4.4: Reconstructed corrected electron vertex for all targets. Note that the thick Aluminum target was run with the cryo-target cell empty.

4.2.1   Background to the Cryo-Target

The 2 cm long cryo-target cell consists of Aluminum entrance and exit windows which together are equivalent to 2.5% of the luminosity of the Deuterium target [9]. Two approaches can be used to remove the background events when calculating the cryo-target yield: a vertex cut can be applied outside the target cell and then the background subtracted using the empty

target runs bin-by-bin in Bjorken-X; or the walls can be removed by a vertex cut in the center of the liquid target.

For the QE events, there are not enough statistics for a good background subtraction. So, a 1 cm long cut (i.e. $\pm 0.5\,cm$) is applied in the middle of the liquid target. This cut is justified by figure 4.5. In this figure, the red points show the yield scaled up to the full cryo-target length (i.e. 2 cm) for different cut widths inside the target; the blue points show the yield when cutting outside the target and subtracting the empty target. Even after subtraction, the normalized yield is not stable outside the target; but the normalized yield is stable for all cuts less than 1 cm.
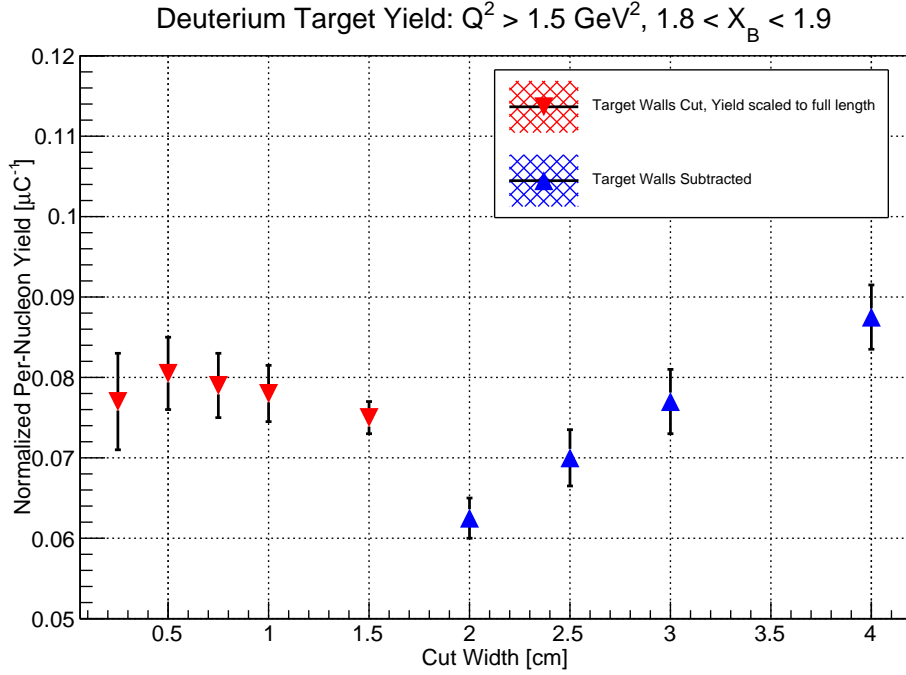
Figure 4.5: Normalized electron yield from the Deuterium target. We apply a cut on Q^2 here (which is discussed in section 5.2 on the QE cuts) and look at a specific range in Bjorken-X. The results are similar for other Bjorken-X bins.

For the DIS events, we have sufficient statistics to perform a background subtraction. In this case, we apply a vertex cut with a full width of 3 cm and subtract the empty target contribution bin-by-bin in Bjorken-X. As can

be seen in figure 4.6, the normalized yield after the background subtraction is more stable than in the QE case.
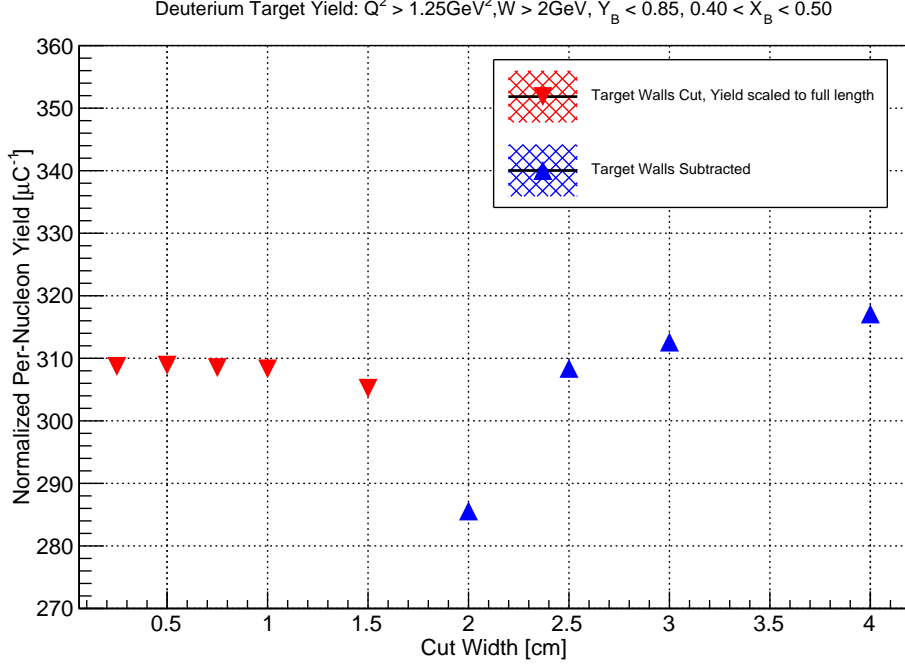
Figure 4.6: Normalized electron yield from the Deuterium target. We apply a DIS cut here (which is discussed in section 5.2) and look at a specific range in Bjorken-X. The results are similar for other Bjorken-X bins.

4.2.2 Background to the Solid Targets

We determined any background to the solid targets by looking at runs where only the Deuterium cryo-target was present. In figure 4.7, we show the reconstructed electron vertex using a DIS cut. The vertex cut used to select the solid target is shown by the red lines. As can be seen there is some background present where the solid target would be located. By normalizing on beam charge and live-time, we determined this background to account for 0.45-0.85% of the yield from the various solid targets run concurrently with Deuterium. (For the thick Aluminum target run with the empty cryo-target cell, the background was about 0.1%).

We performed a similar analysis for the QE events (figure 4.8). Here we do not see any background under the solid target, and do not perform any subtraction.

Figure 4.7: Reconstructed DIS electron vertex when only the Deuterium cryo-target is located in the beam-line. We apply a DIS cut (see section 5.2). When the solid target is present, we select events from the solid target with the vertex cut shown by the red lines.

Figure 4.8: Reconstructed QE electron vertex when only the Deuterium cryo-target is located in the beam-line. We apply a QE cut (see section 5.2). When the solid target is present, we select events from the solid target with the vertex cut shown by the red lines.
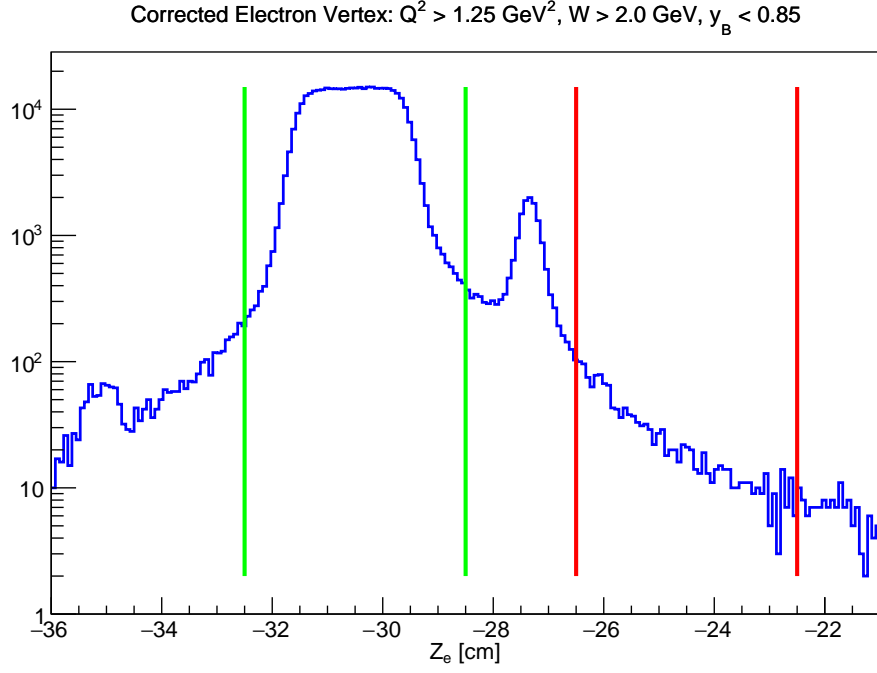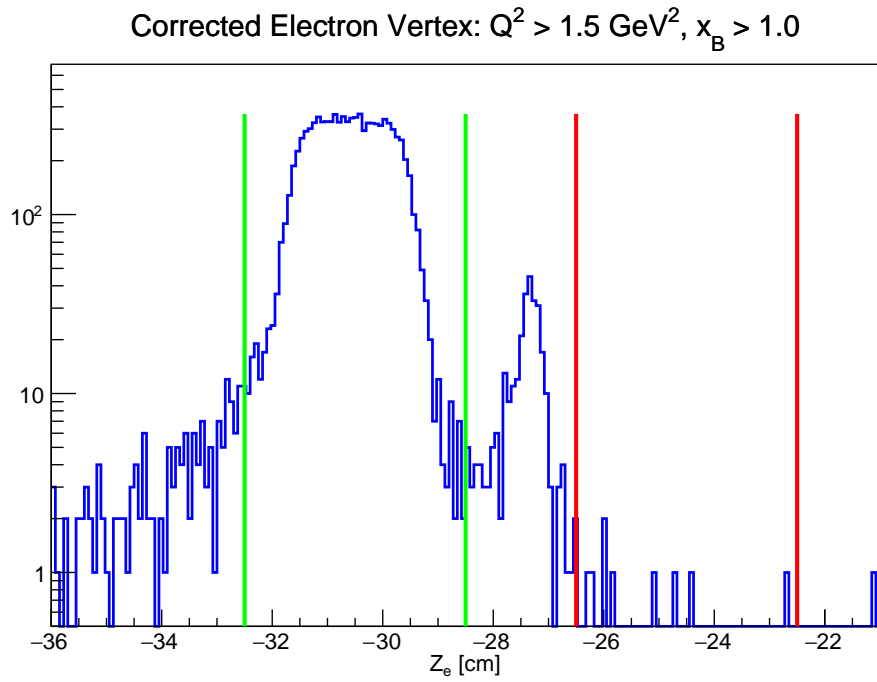
Chapter 5

Cross-Section Ratio Extraction

5.1 Method of Cross-Section Ratio Extraction

Unlike in a small-acceptance spectrometer which measures a cross-section at nearly a fixed angle and with a small momentum bite, the $CLAS$ detector has a large acceptance. We wish to calculate cross-sections at fixed Bjorken-X values. The cross-section is differential with respect to two independent variables (e.g. $\frac{d^2\sigma}{d\Omega dE}$ or $\frac{d^2\sigma}{dx dQ^2}$). When we calculate the cross-section ratios at a given Bjorken-X, we are integrating over whatever range in Q^2 is kinematically allowed by the beam energy, detector acceptance, and our cuts. This integration over Q^2 is not a problem because the EMC ratios and a_2 values are known to be Q^2 independent (above a certain threshold) [1, 2, 3].

The procedure to extract the cross-section ratios is then as follows. The data are first binned in Bjorken-X. Every event in a given Bjorken-X bin is given the following weight:

$$Weight = \frac{BC \times RC \times CC \times ISO}{NORM \times ACC}.$$
(5.1)

In equation 5.1, $NORM$ is the standard luminosity factor, which is equal to the beam-charge times the target thickness divided by the live-time. ACC is the acceptance correction factor, which will be discussed in section 5.3. BC is the bin centering correction. It is defined as the ratio of the radiated model cross-section (section 5.4) at the bin center to the cross-section at the event location. That is,

$$BC = \frac{\sigma_{Rad}(x_{center}, Q^2_{event})}{\sigma_{Rad}(x_{event}, Q^2_{event})}.$$ (5.2)

The term RC in equation 5.1 is the radiative correction factor; the radiative corrections are discussed in section 5.5. The term CC is the coulomb correction factor; the coulomb corrections are discussed in section 5.6. The term ISO refers to the isoscalar corrections, which are applied to the DIS cross-section ratios only; the isoscalar corrections are discussed in section 5.7.

5.2 Kinematic Selection Cuts

To calculate the inclusive DIS cross-section ratios, we have to select a set of cuts on the standard kinematic variables (figure 5.1). To do this, we make use of the $CLAS$ simulation. We uniformly generate electrons in energy and solid angle from the corresponding target location. Then, for every generated event, we apply a weight using our model DIS cross-section described in section 5.4 [23]. We generate a grid of our model cross-section at fixed values of Q^2 and Bjorken-X. We then radiate the model cross-section [20] to get a radiated cross-section at each grid point. For every generated event, we perform a 2-dimensional linear interpolation to calculate the radiated cross-section at the specific Q^2 and Bjorken-X value.

In figure 5.2a, we show four kinematic variables $(Q^2, W, X_B \, and \, Y_B = \frac{\nu}{E_{Beam}})$ for the Deuterium data compared to the weighted Deuterium DIS simulation. We begin by applying a cut above the resonance region at $W > 1.8 GeV$. Using the resultant distributions (figure 5.2b), we then select a cut on Q^2 based on where the data and reconstructed simulation begin to match well. After applying a cut of $Q^2 > 1.50 GeV^2$ (figure 5.2c), we apply a cut of $Y_B < 0.85$. This Y_B cut is equivalent to requiring the scattered electron to have a momentum greater than about 750 MeV/c. After all these cuts are applied, the data and the reconstructed simulation match quite nicely (figure 5.3).

For the QE case, we are interested in the range $0.8 < X_B < 2.0$ (primarily in the plateau region from $1.4 < X_B < 2.0$. It is also known that we need to apply a cut of $Q^2 > 1.5 GeV^2$ in order to select nucleons with high momentum [3]. In figure 5.4, we compare the radiated QE model cross-section to the data for the Carbon target.
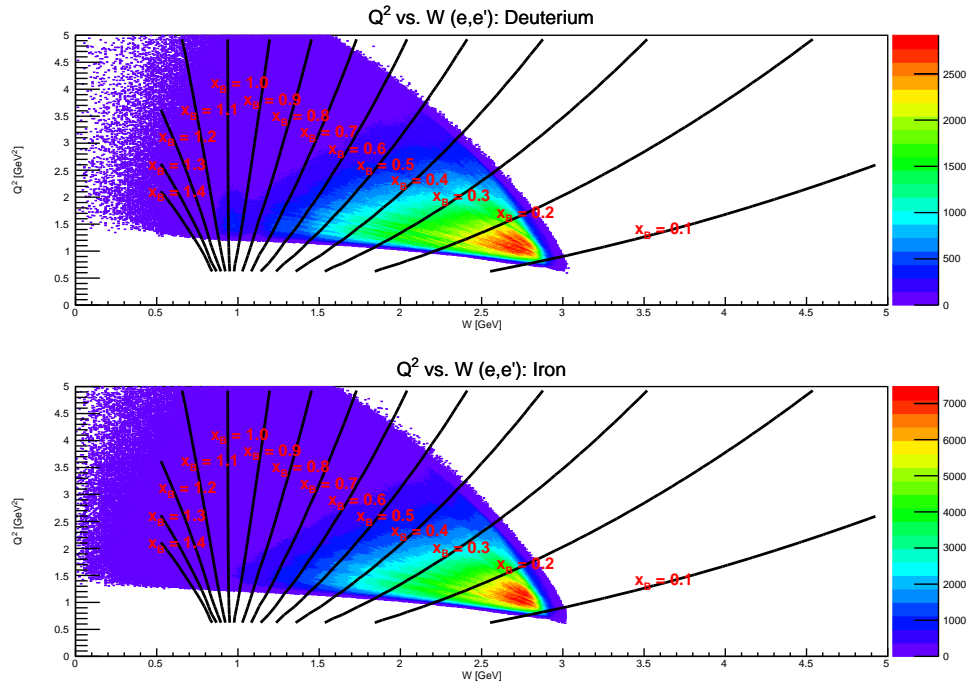
Figure 5.1: Q^2 vs. Invariant Mass with Bjorken-X contours for (e,e') events. Top: Deuterium Target. Bottom: Iron Target.
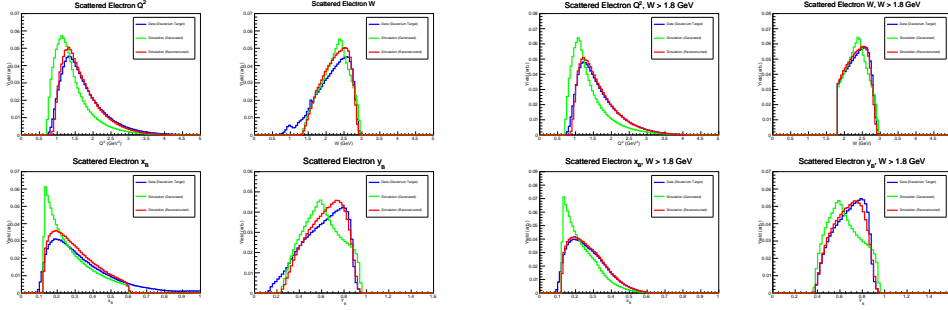
(a) No Kinematic Cuts

(b) $W > 1.8 GeV$
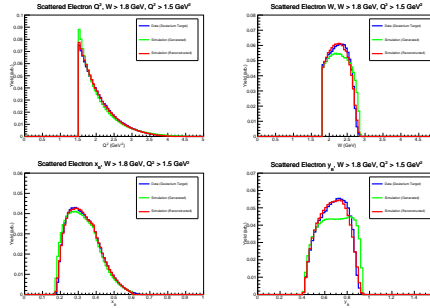
(c) $W > 1.8 GeV \, \& \, Q^2 > 1.50 GeV^2$

Figure 5.2: Comparison of data and DIS model cross-section radiated. The green curves are the generated events in the simulation; the red curves are the accepted and reconstructed events in the simulation; the blue curves are the data from the Deuterium target. The yields are arbitrarily normalized here, so only the shape is compared. Clockwise from Top Left: Q^2, W, Y_B, X_B.
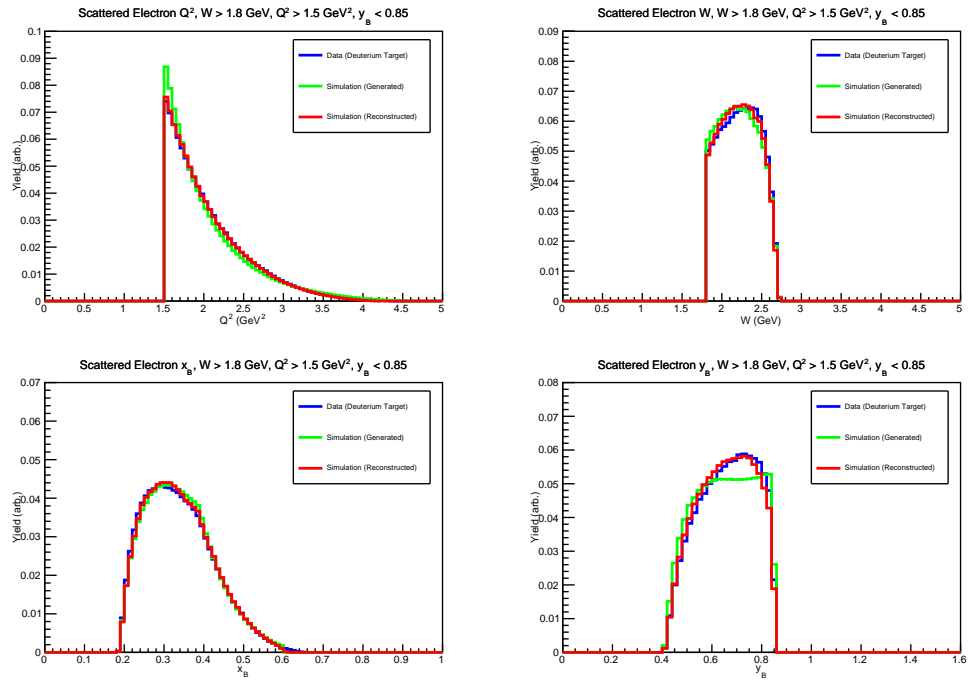
Figure 5.3: Same as figure 5.2a, except now with a cut of $W > 1.8 GeV$, $Q^2 > 1.50 GeV^2$ & $Y_B < 0.85$ applied.

Figure 5.4: Comparison of data and QE model cross-section radiated. The green curves are the generated events in the simulation; the red curves are the accepted and reconstructed events in the simulation; the blue curves are the data from the Carbon target. The yields are arbitrarily normalized here, so only the shape is compared. We apply a cut here of $Q^2 > 1.5 GeV^2 \& 0.8 < X_B < 2.0$ Left: Q^2 Right: X_B.
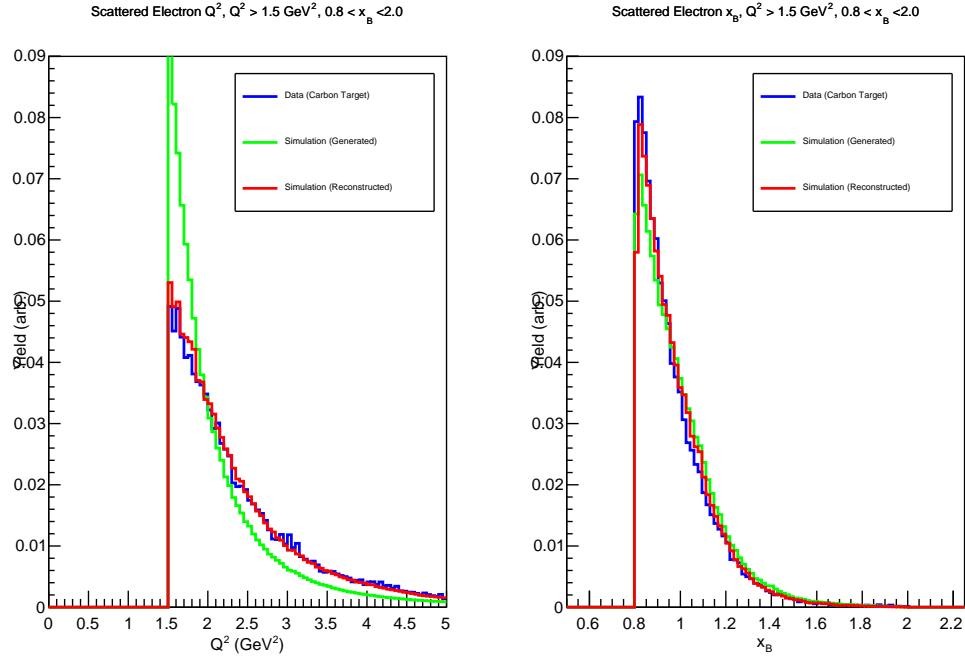
5.3   Acceptance Corrections

Acceptance corrections were applied using the standard *CLAS* simulation (GSIM, GPP, and RECSIS) [10], with the *EG2c* efficiency maps and calculated resolutions included. Electrons were generated uniformly in solid angle and energy from both the liquid and solid target locations. For the DIS region acceptance correction, the simulated data was binned in Q^2 and W; for the QE region acceptance correction, the data was binned in Q^2 and X_B. For every such bin the *ACC* term in equation 5.1 is calculated as

$$ACC = \frac{N_{Accepted}}{N_{Generated}}. \tag{5.3}$$

The binning is chosen so that the standard binomial uncertainty for all bins (except at the edges of the acceptance) is less than 0.75% for the DIS acceptance (3.0% for the QE acceptance). The extracted DIS acceptance maps for the Deuterium and solid targets are shown in figure 5.5; the QE acceptance maps for the Deuterium and solid targets are shown in figure 5.6.

(a) Deuterium Target   (b) Solid Target
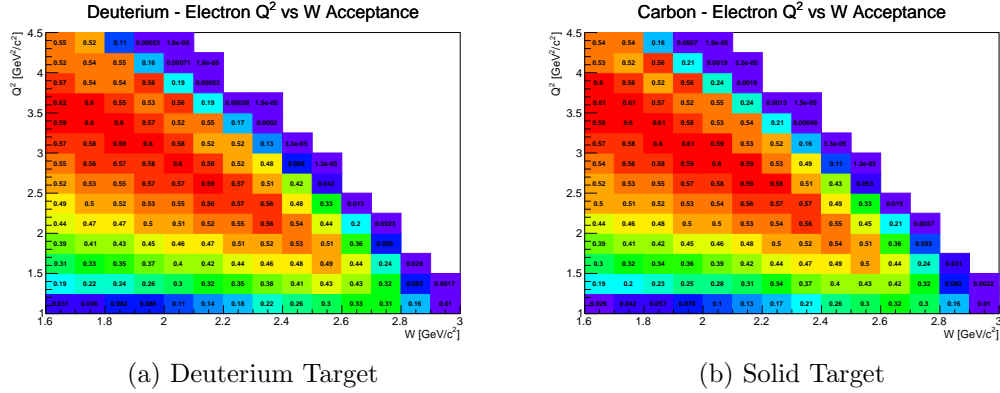
Figure 5.5: Acceptance correction factors in the DIS region.
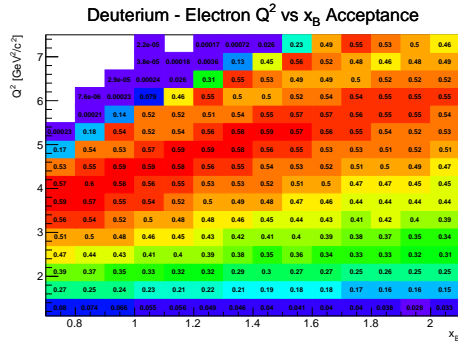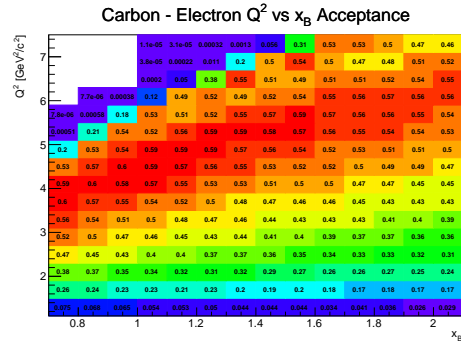
(a) Deuterium Target   (b) Solid Target

Figure 5.6: Acceptance correction factors in the QE region.

5.4 Model Cross-Section

Model cross-sections for both the DIS and QE region are taken from the code *INCLUSIVE* [23]. These model cross-sections are used to determine the kinematic cuts, for the bin-centering corrections, for the radiative corrections, and for the coulomb corrections. The DIS (QE) model cross-sections are shown for all targets in figure 5.7 (5.8). As discussed previously the model cross-sections are generated on a two-dimensional grid, and are linearly interpolated to determine the model cross-section at any location between the grid points.
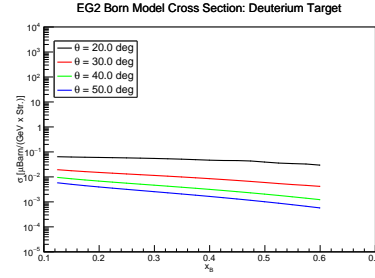
(a) Deuterium Target
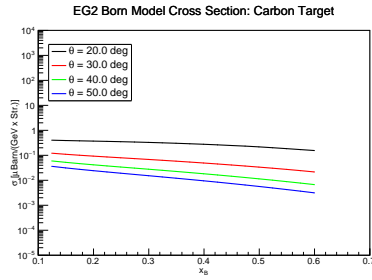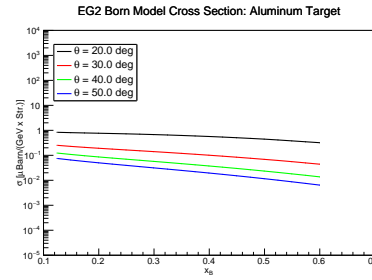
(b) Carbon Target

(c) Aluminum Target

(d) Iron Target

(e) Lead Target

Figure 5.7: DIS model cross-sections for the five targets as a function of X_B for various θ values.

(a) Deuterium Target

(b) Carbon Target

(c) Aluminum Target

(d) Iron Target
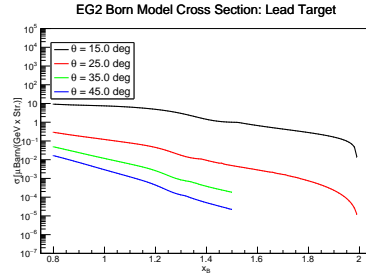
(e) Lead Target

Figure 5.8: QE model cross-sections for the five targets as a function of X_B for various θ values.

5.5   Radiative Corrections

Radiative corrections must be applied to obtain the born cross-sections. As described in reference [20], an unfolding procedure can be used to extract the born cross-section from the measured radiated cross-section. In our case, this is obviously not practical, and a different procedure had to be used. Inside the code *INCLUSIVE* [23], the model cross-sections are internally and externally radiated according the prescription given in reference [20]. Then a correction factor can be calculated for any electron scattering angle and energy (or X_B and Q^2). The radiative correction factor is defined as the ratio of the model born to the radiated cross-section:

$$RC = \frac{\sigma_{Born}}{\sigma_{Rad}}.$$ (5.4)

In equation 5.1, the born and radiated cross-sections are evaluated at the X_B bin center and the measured Q^2 value, since the bin centering corrections are applied using the radiated model cross-sections.

In figure 5.9 (5.10), we show the radiative correction factors as a function of X_B in the DIS (QE) region.
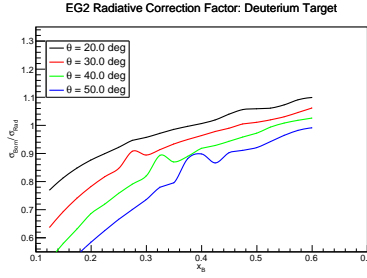
(a) Deuterium Target
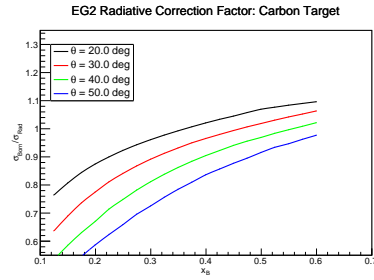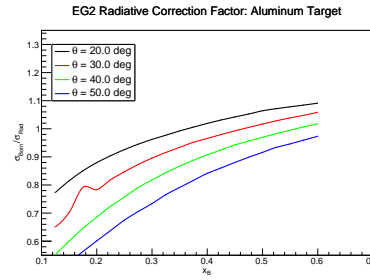
(b) Carbon Target
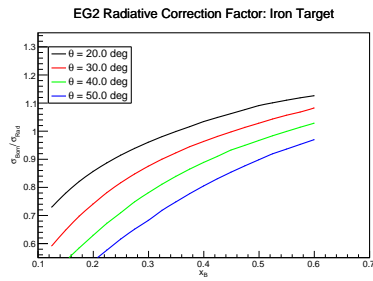
(c) Aluminum Target
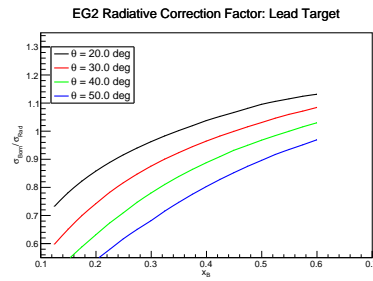
(d) Iron Target

(e) Lead Target

Figure 5.9: DIS Radiative correction factors for the five targets as a function of X_B for various θ values.
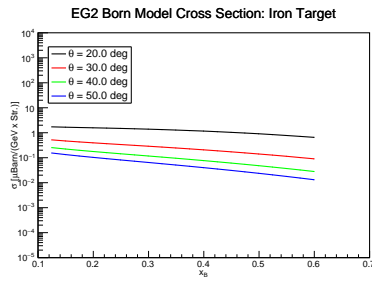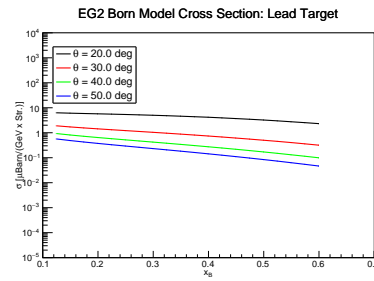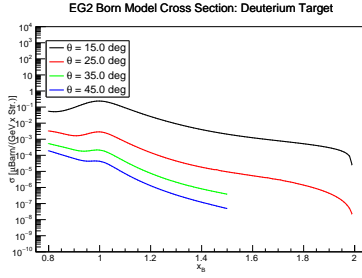
71
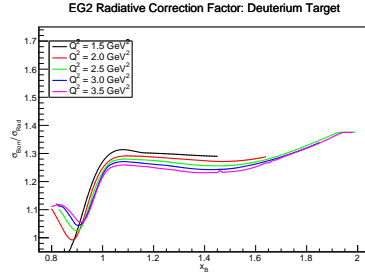
(a) Deuterium Target
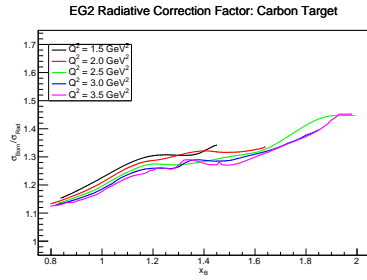
(b) Carbon Target
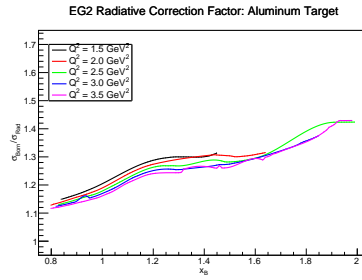
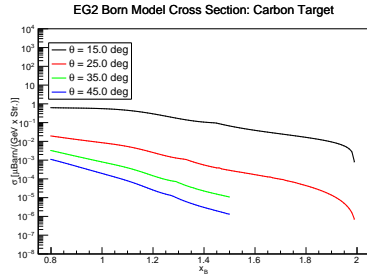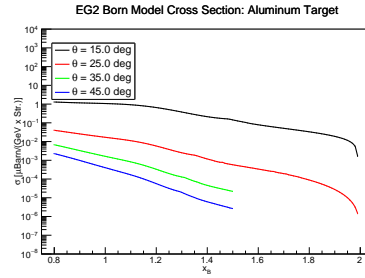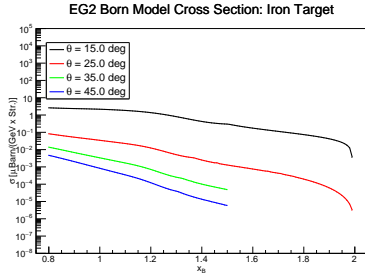(c) Aluminum Target
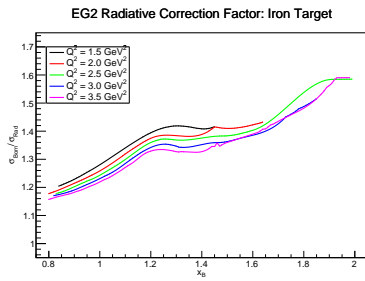
(d) Iron Target
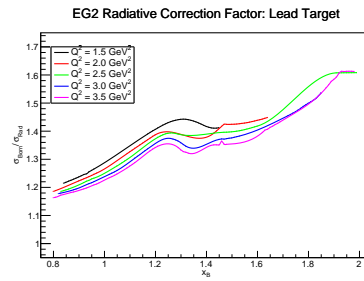
(e) Lead Target

Figure 5.10: QE Radiative correction factors for the five targets as a function of X_B for various Q^2 values.

5.6 Coulomb Corrections

The initial (scattered) electron is accelerated (decelerated) by the coulomb field of the nucleus. This means that the measured beam energy and scattered momentum are not equivalent to the values at the reaction vertex. In the Effective Momentum Approximation (EMA) [24] approach, both the initial and final electron's energies at the reaction vertex are higher by an amount ΔE than the measured values. The EMA approach has been well validated in the QE region; for the DIS region, recent work [25] suggests that the EMA approach is also reasonable.

The calculation of ΔE was done by a previous, approved *EG2c* analysis [11], and we take the ΔE from there. The calculated ΔE values are shown in table 5.1.

Target	$\Delta E\,[MeV]$
^2D	0
^{12}C	2.9
^{27}Al	5.6
^{56}Fe	9.4
^{208}Pb	20.3

Table 5.1: Coulomb correction ΔE values calculated using the Effective Momentum Approximation (EMA).

Once ΔE is known, we can calculate the the coulomb correction factor in equation 5.1 as the ratio of the model cross-sections at the un-shifted and shifted kinematics times the focusing factor [24]. That is,

$$CC = \frac{\sigma_{Born}(E, E', \theta)}{\sigma_{Born}(E + \Delta E, E' + \Delta E, \theta)} \times \left(\frac{E}{E + \Delta E}\right)^2. \qquad (5.5)$$

In equation 5.5, E, E' and θ are calculated at the bin center. This coulomb correction factor for all targets in the DIS (QE) region is shown in figure 5.11 (5.12).
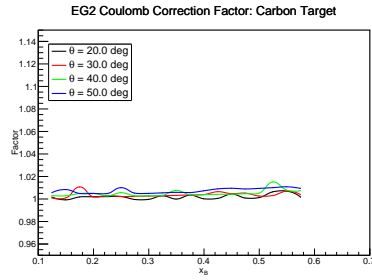
(a) Carbon Target
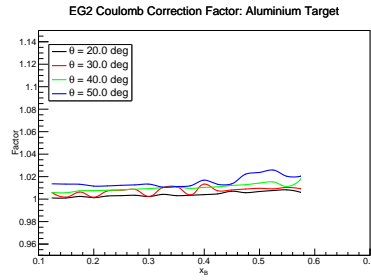
(b) Aluminum Target
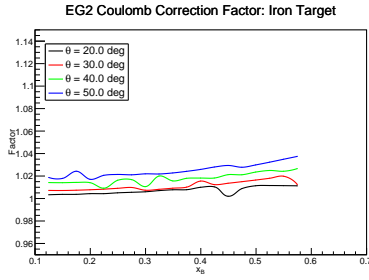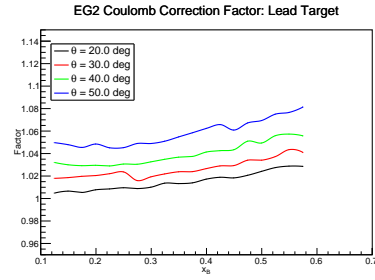
(c) Iron Target

(d) Lead Target

Figure 5.11: DIS Coulomb correction factors for the five targets as a function of X_B for various θ values.
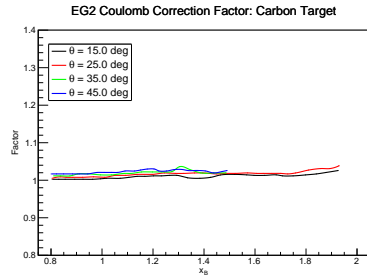
(a) Carbon Target
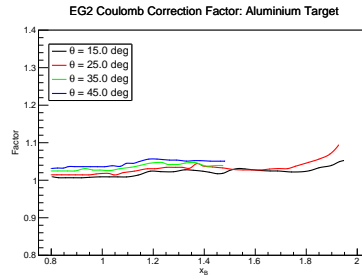
(b) Aluminum Target
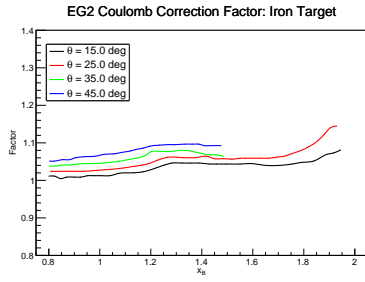
(c) Iron Target
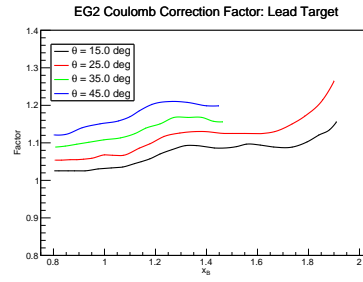
(d) Lead Target

Figure 5.12: QE Coulomb correction factors for the five targets as a function of X_B for various θ values.

5.7   Isoscalar Corrections for DIS Events

Previous studies of the EMC effect [26, 27] have included an isoscalar correction factor to account for the unequal number of protons and neutrons in many nuclei. This correction factor will adjust the measured cross-section per nucleon for a nucleus A to a new value which represents the cross-section per nucleon for a nucleus A with an equal number of neutrons and protons. This correction factor is given by

$$ISO = \frac{\frac{A}{2} \cdot \left(1 + \frac{\sigma_n}{\sigma_p}\right)}{Z + N \cdot \frac{\sigma_n}{\sigma_p}} \tag{5.6}$$

In reference [26] for the neutron to proton cross-section ratio as a function of Bjorken-X was simply paramerized as $\frac{\sigma_n}{\sigma_p} = 1 - 0.8 \cdot X_B$. Here we use the updated parametrization from [27] (figure 5.13). In figure 5.14 we show the applied isoscalar correction factors for the various nuclei in this experiment using this updated parametrization.
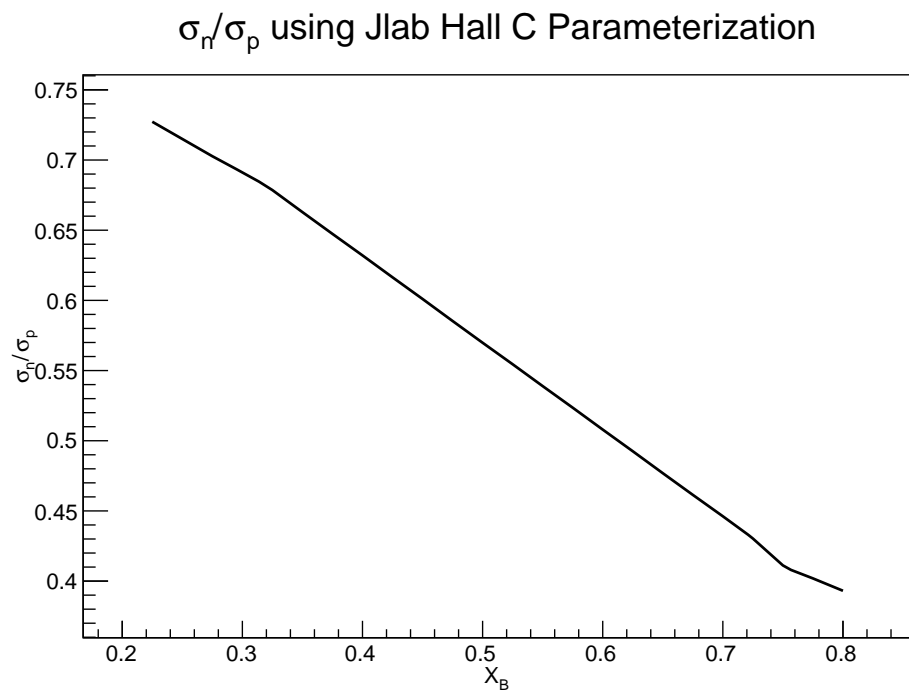
Figure 5.13: Neutron to proton cross-section ratio as a function of Bjorken-X taken from [27].
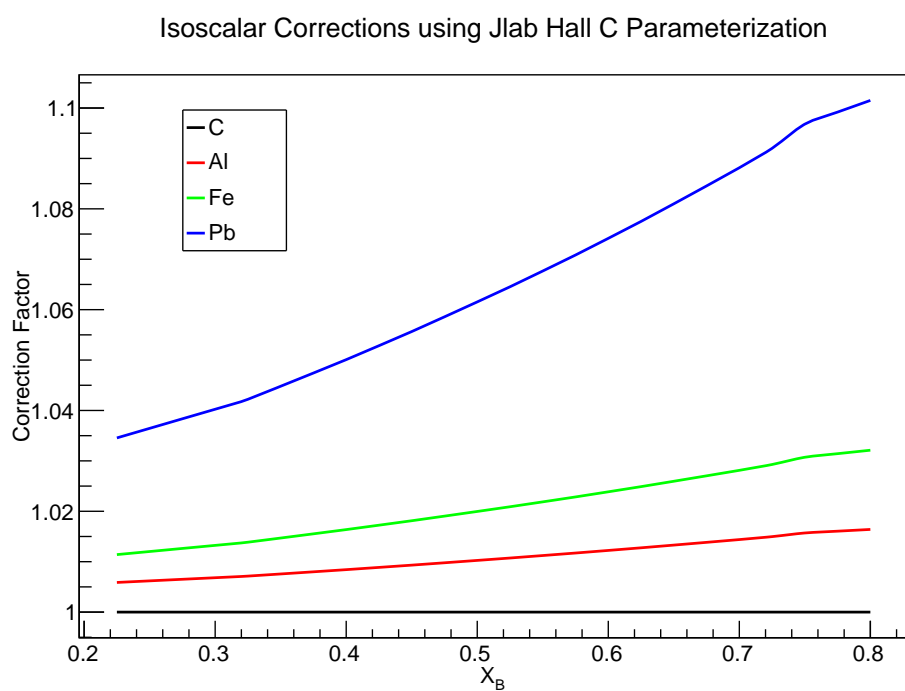
Figure 5.14: Applied isoscalar correction factors for all solid targets using the parametrization in figure 5.13.

Chapter 6

Final Results

6.1 DIS Cross-Section Ratios and EMC Slopes

The final per-nucleon cross-section ratios are shown in figure 6.1. A kinematic cut of $Q^2 > 1.5 GeV^2$, $W > 1.8 GeV$, and $Y_B < 0.85$ is applied. The data is divided into Bjorken-X bins of width 0.04. The data covers a range of 0.20-0.60 in Bjorken-X. A table with the measured ratios and the associated uncertainties is shown in table 6.1. We apply a linear fit to the data from 0.26-0.54 to obtain the EMC slope for each nucleus. These slopes are shown in table 6.2. In order to determine the stability of our slopes to the kinematic cuts, we recalculated the slopes and ratios for different cuts on Q^2 and W. The slopes for the different kinematic cuts are shown in table 6.3; the results are consistent within the uncertainties.

Figure 6.1: Measured DIS per-nucleon cross-section Ratios to Deuterium for (clockwise from top-left) Carbon, Aluminum, Lead and Iron. The error bars on the individual points are the combined statistical and point-to-point systematic uncertainties. The normalization uncertainty is stated for each ratio on the corresponding plot. The plotted published data comes from reference [26].

X_B	$\frac{\sigma(C)}{\sigma(D)}$ Norm. 1.81%	$\frac{\sigma(Al)}{\sigma(D)}$ Norm. 1.82%	$\frac{\sigma(Fe)}{\sigma(D)}$ Norm. 1.83%	$\frac{\sigma(Pb)}{\sigma(D)}$ Norm. 1.94%
0.22	1.056 ± 0.051	1.027 ± 0.050	1.041 ± 0.052	1.049 ± 0.051
0.26	1.016 ± 0.008	1.001 ± 0.008	1.014 ± 0.008	1.010 ± 0.008
0.30	0.997 ± 0.008	0.993 ± 0.008	0.999 ± 0.008	0.995 ± 0.008
0.34	0.994 ± 0.008	0.990 ± 0.008	0.992 ± 0.008	0.987 ± 0.008
0.38	0.985 ± 0.008	0.980 ± 0.008	0.979 ± 0.008	0.975 ± 0.008
0.42	0.971 ± 0.007	0.967 ± 0.007	0.960 ± 0.008	0.955 ± 0.007
0.46	0.949 ± 0.007	0.947 ± 0.007	0.936 ± 0.007	0.921 ± 0.007
0.50	0.936 ± 0.007	0.933 ± 0.007	0.920 ± 0.007	0.911 ± 0.007
0.54	0.929 ± 0.007	0.912 ± 0.008	0.905 ± 0.007	0.894 ± 0.007
0.58	0.884 ± 0.044	0.862 ± 0.042	0.856 ± 0.043	0.786 ± 0.110

Table 6.1: Measured DIS per-nucleon cross-section ratios for Carbon, Aluminum, Iron, and Lead to Deuterium. The error given for each point is the combined statistical and point-to-point uncertainty. The normalization uncertainty for a each ratio is stated at the top of the table.

Target	$|Slope|$	$\chi^2/$Ndf	Published $|Slope|$
^{12}C	0.316 ± 0.030	2.7/6	0.292 ± 0.023
^{27}Al	0.318 ± 0.030	5.7/6	-
^{56}Fe	0.404 ± 0.031	2.9/6	0.388 ± 0.032
^{208}Pb	0.434 ± 0.030	6.1/6	$0.409 \pm 0.039\,(^{197}Au)$

Table 6.2: Measured EMC slopes from the fit in figure 6.1. The uncertainties shown in the table are the combination of the fit uncertainties and normalization uncertainties. Published values are taken from [5].

Applied Q^2, W Cut	Fit Range	C/D $\lvert Slope\rvert$	Al/D $\lvert Slope\rvert$	Fe/D $\lvert Slope\rvert$	Pb/D $\lvert Slope\rvert$
$Q^2 > 1.5 GeV^2$ $W > 1.8 GeV$	0.26-0.54	0.316 ± 0.030	0.318 ± 0.030	0.404 ± 0.031	0.434 ± 0.030
$Q^2 > 1.5 GeV^2$ $W > 2.0 GeV$	0.26-0.50	0.329 ± 0.037	0.351 ± 0.038	0.405 ± 0.038	0.445 ± 0.036
$Q^2 > 1.25 GeV^2$ $W > 1.8 GeV$	0.26-0.54	0.348 ± 0.030	0.342 ± 0.030	0.424 ± 0.030	0.446 ± 0.030
$Q^2 > 1.25 GeV^2$ $W > 2.0 GeV$	0.26-0.50	0.367 ± 0.037	0.358 ± 0.039	0.409 ± 0.038	0.436 ± 0.037

Table 6.3: Measured EMC slopes for different kinematic cuts. The uncertainties shown in the table are the combination of the fit uncertainties and normalization uncertainties.

6.2 QE Cross-Section Ratios and a_2 Values

The final per-nucleon cross-section ratios are shown in figure 6.2. The data is divided into 20 equally sized bins in Bjorken-X in the range 0.8-2.0. We apply a kinematic cut of $Q^2 > 1.5 GeV^2$. A table with the measured ratios and the associated uncertainties is shown in table 6.4. We take a weighted average of the ratios from 1.529-1.871 for each nucleus (1.614-1.871 for Lead); these measured a_2 values are shown in table 6.5.
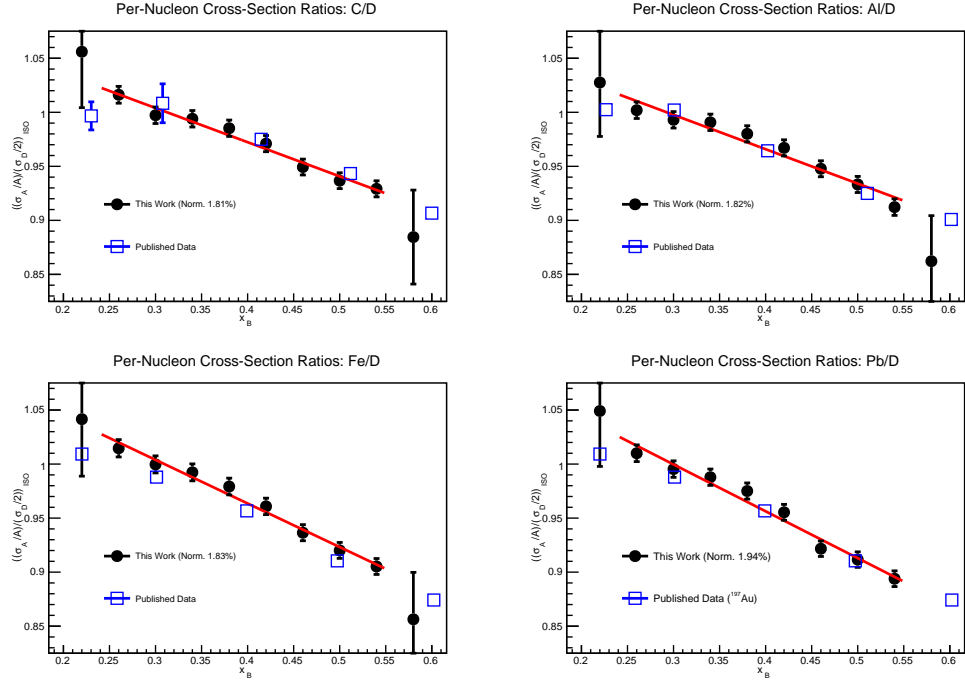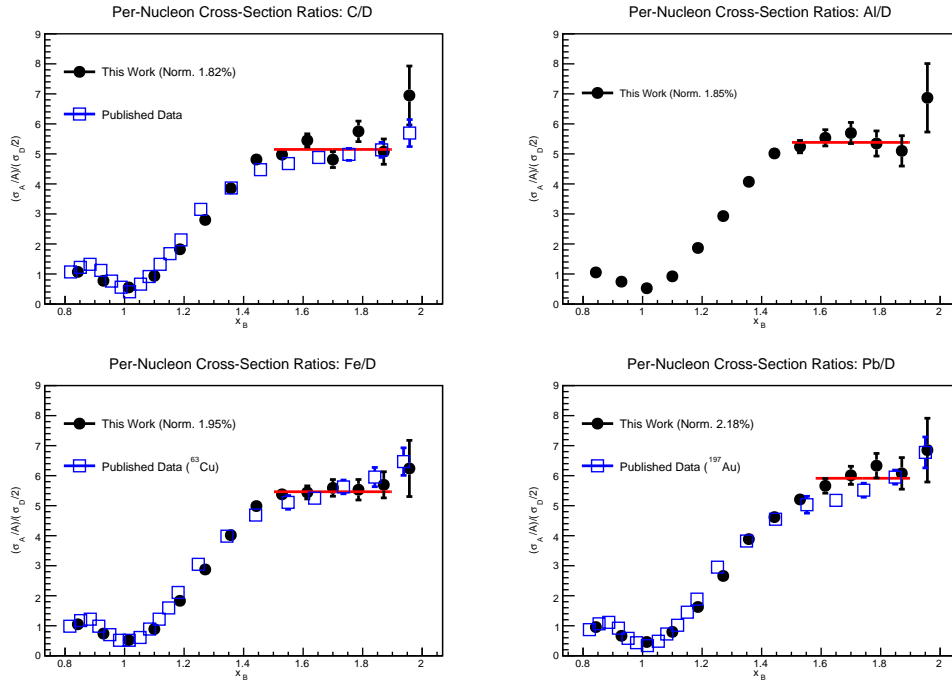

Figure 6.2: Final QE cross-section Ratios to Deuterium for (clockwise from top-left) Carbon, Aluminum, Lead and Iron. The error bars on the individual points are the combined statistical and point-to-point systematic uncertainties. The normalization uncertainty is stated for each ratio on the corresponding plot. The plotted published data comes from reference [28].

X_B	$\frac{\sigma(C)}{\sigma(D)}$ Norm. 1.82%	$\frac{\sigma(Al)}{\sigma(D)}$ Norm. 1.85%	$\frac{\sigma(Fe)}{\sigma(D)}$ Norm. 1.95%	$\frac{\sigma(Pb)}{\sigma(D)}$ Norm. 2.18%
0.843	1.069 ± 0.023	1.052 ± 0.022	1.049 ± 0.022	0.956 ± 0.020
0.929	0.773 ± 0.016	0.744 ± 0.016	0.739 ± 0.016	0.665 ± 0.014
1.014	0.552 ± 0.012	0.525 ± 0.011	0.520 ± 0.011	0.459 ± 0.010
1.100	0.936 ± 0.020	0.921 ± 0.020	0.889 ± 0.019	0.796 ± 0.017
1.186	1.823 ± 0.041	1.867 ± 0.043	1.831 ± 0.040	1.625 ± 0.037
1.271	2.801 ± 0.066	2.929 ± 0.074	2.875 ± 0.066	2.659 ± 0.064
1.357	3.852 ± 0.098	4.071 ± 0.113	4.018 ± 0.100	3.886 ± 0.102
1.443	4.814 ± 0.139	5.016 ± 0.162	4.987 ± 0.139	4.619 ± 0.139
1.529	4.975 ± 0.166	5.242 ± 0.206	5.378 ± 0.170	5.207 ± 0.182
1.614	5.450 ± 0.218	5.536 ± 0.270	5.442 ± 0.217	5.207 ± 0.244
1.700	4.811 ± 0.265	5.697 ± 0.352	5.593 ± 0.278	5.661 ± 0.302
1.786	5.751 ± 0.341	5.347 ± 0.418	5.531 ± 0.341	6.011 ± 0.407
1.871	5.076 ± 0.421	5.101 ± 0.506	5.695 ± 0.435	6.333 ± 0.526
1.957	6.947 ± 0.980	6.869 ± 1.140	6.240 ± 0.936	6.851 ± 1.060

Table 6.4: Measured QE per-nucleon cross-section ratios for Carbon, Aluminum, Iron, and Lead to Deuterium. The error given for each point is the combined statistical and point-to-point uncertainty. The normalization uncertainty for a each ratio is stated at the top of the table.

Target	a_2	χ^2/Ndf	Published a_2
^{12}C	5.15 ± 0.14	$7.7/4$	4.75 ± 0.16
^{27}Al	5.38 ± 0.17	$1.9/4$	-
^{56}Fe	5.46 ± 0.15	$0.8/4$	$5.21 \pm 0.18 \left(^{63}Cu\right)$
^{208}Pb	5.91 ± 0.21	$2.3/3$	$5.16 \pm 0.22 \left(^{197}Au\right)$

Table 6.5: Measured a_2 values from the fit in figure 6.2. The uncertainties shown in the table are the combination of the fit uncertainties and normalization uncertainties. Published values are taken from [5].

6.3 Systematic Uncertainties

The systematic uncertainties are divided into two groups: the point-to-point uncertainties are uncorrelated between different bins and are treated in the same manner as the statistical uncertainties; the normalization uncertainties affect the overall scale but do not vary between kinematic points.

In table 6.6 (6.7), the sources of systematic uncertainties and their effect on the final per-nucleon cross-section ratios are shown for DIS (QE) events. These uncertainties are discussed in some detail in the following subsections.

Source	Point-to-Point (%)	Normalization (%)
Beam Charge/ Time-Dependent Instabilities	-	1.0
Target Thickness and Cuts	-	1.42-1.58
Acceptance Corrections	0.6 (5)	-
Radiative Corrections	-	0.5
Coulomb Corrections	-	0.1
Bin-Centering Corrections	0.5	-
Total	0.78	1.81-1.94

Table 6.6: Sources of systematic uncertainties on the final DIS ratios, and their relative contributions. For the acceptance uncertainty, the value listed in the parenthesis are for the first and last Bjorken-X bins.

6.3.1 Beam Charge and Time-Dependent Instabilities

Since we combine all the Deuterium runs when calculating the cross-section ratios, we are sensitive to changes in the beam charge monitoring devices, fluctuations in the cryo-target, and changes to the *CLAS* detector over the run period. Since this uncertainty will affect all points in the same way, it is a normalization uncertainty. The simplest way to estimate this uncertainty is by looking at the systematic changes in the normalized yield for the Deuterium target in figure 4.1.

We first make histogram of the percent deviation of the normalized yield for every run from the mean weighted yield for all runs (figure 6.3). The fitted width of the main peak in this plot is approximately 0.65%. In addition, we see that certain groups of runs are systematically shifted from the

Source	Point-to-Point (%)	Normalization (%)
Beam Charge/ Time-Dependent Instabilities	-	1.0
Target Thickness and Cuts	-	1.42-1.58
Acceptance Corrections	1.2 (2.5, 10)	-
Radiative Corrections	-	0.5
Coulomb Corrections	-	0.2-1.0
Bin-Centering Corrections	0.5	-
Bin Migration	1.7	-
Kinematic Corrections	0.3	-
Total	2.16	1.82-2.18

Table 6.7: Sources of systematic uncertainties on the final QE ratios, and their relative contributions. For the acceptance uncertainty, the values listed in the parenthesis are for the last two Bjorken-X bins.

weighted mean of the yield by up to a few percent. So, we choose to place an uncertainty of 1% on the ratio because of this.

6.3.2 Target Thickness and Vertex Cuts

We place a normalization uncertainty on our measured ratios due to the target thicknesses and software vertex cuts.

The uncertainty in the *EG2c* cryo-target thickness has been estimated to be 1.0% [29]. The thicknesses of the solid targets were measured to about the 1 micron level [9]. This translates to a relative uncertainty of 0.1-0.7%.

For the solid targets, since we apply a vertex cut much larger than the solid target reconstruction resolution, there is no significant cut uncertainty.

For the cryo-targets, in the DIS case we apply a vertex cut around the Deuterium target with a full width of 3 cm. We vary this cut by 0.25 cm and look at the change in the windows-subtracted yield in each Bjorken-X bin. We find that the yield always increases with a wider cut for all bins. The maximum change in the yield is 1.0%, and we take this as the normalization uncertainty.

In the QE case, we apply a cut of 1 cm in the center of the cryo-target. The main question here concerns the reconstruction 'optics' (i.e. is the 2 cm long cryo-target really reconstructed to the correct length?). To test this, we

Normalized Yield Percent Deviation from Weighted mean
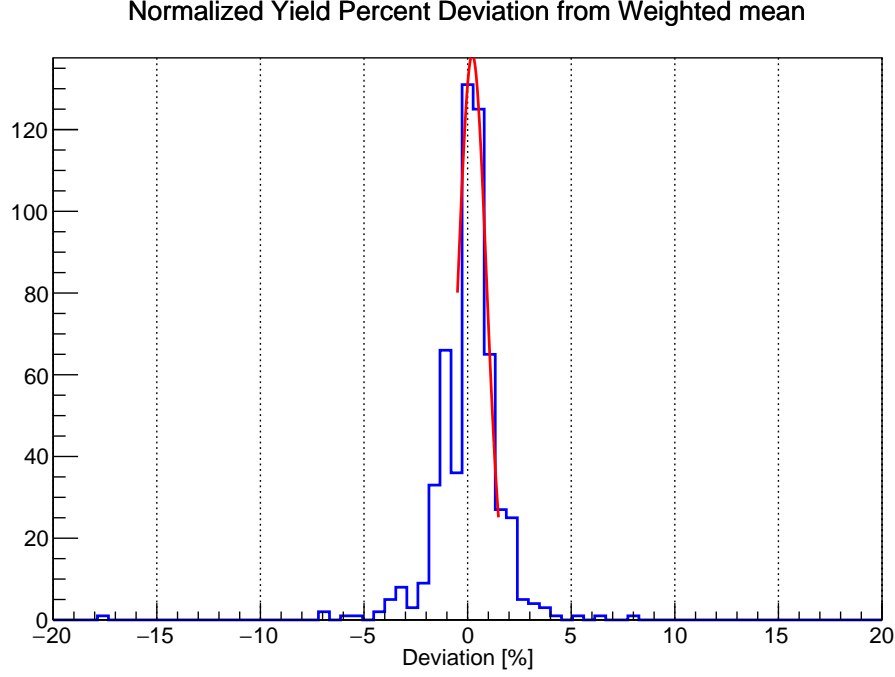
Figure 6.3: Percent deviation from the mean of the charge normalized Deuterium yield for every run. We find that the width of the main peak is approximately 0.65%.

look at the reconstructed window locations for the empty target runs (figure 4.4) and compare to the ideal target length. We make Gaussian fits to the two target foils for the empty target runs, and calculate the deviation of the difference in the fit means from the ideal target length. We repeat this fit several times with different ranges around the peaks, and monitor how well the peaks are fitted. In figure 6.4, we show the percent deviation from the ideal target length vs. the fit range around each peak. We do not see any region where the deviation is constant. However, the points shown are the ones where the both fit's calculated χ^2 are reasonable, indicating that using a Gaussian fit in reasonable. Given the spread of the points in this range, we place a conservative uncertainty of 1% on our 1 cm cut.

For the effect on the cross-section ratios, we combine the cryo-target thickness, solid-target thickness, and cut uncertainties. This gives a normalization uncertainty of 1.42-1.58% in both the DIS and QE regions.

Figure 6.4: Percent deviation of the target length determined by the fit from the assumed cryo-target length vs. Gaussian fit range around the peak.

6.3.3 Acceptance Corrections

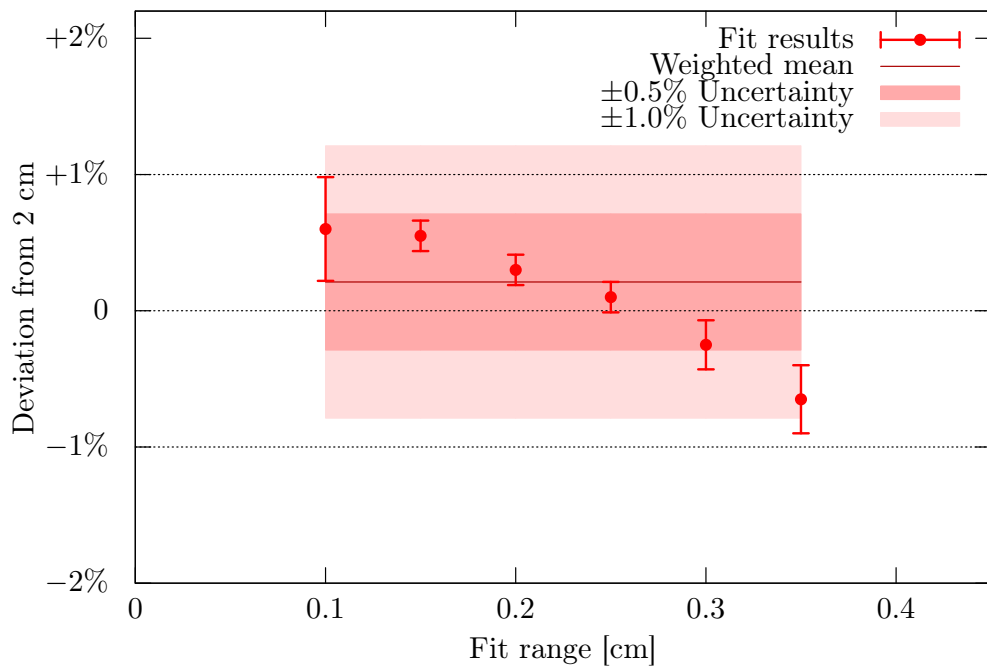We place a point-to-point uncertainty based on the standard binomial uncertainty extracted for the acceptance corrected values. As noted in section 5.3, we limited the uncertainty in the acceptance correction factor to 0.75% (3.0%) in the DIS (QE) region. When summing the data into a one-dimensional function of Bjorken-X, this uncertainty will be decreased roughly by the square-root of the number of bins in the sum. In the DIS (QE) region, for each Bjorken-X point, we have about 9 (16) acceptance bins. This allows us to place an uncertainty of 0.25% (0.75%) on the DIS (QE) region. (The uncertainties are higher near the edges of the acceptance.) Since the acceptance correction factors are applied to the Deuterium and solid target separately, the effect on the cross-section ratios is 0.35% (1.06%) for the DIS (QE) region.

In addition, we place an general point-to-point uncertainty of 0.5% on the simulation. This gives a final point-to-point uncertainty of 0.6% (1.2%) on the acceptance in the DIS (QE) region.

6.3.4 Radiative, Coulomb, and Bin Centering Corrections

Point-to-point radiative correction uncertainties are estimated to contributed about 1% for the absoulte cross-section [26, 30]. These point-to-point uncertainties should cancel in the ratios [26]. The normalization uncertainty on the cross-section ratios due to radiative corrections is estimated to be 0.5% [26, 27].

The coulomb correction range from 0-5% for the DIS region and from 0-15% for the QE region. There is a 10% uncertainty in the coulomb potential [24]. To study the effect of this uncertainty on ΔE on the coulomb correction factors, we recalculate the factors with ΔE changed by 10% [30]. For the DIS region, this changes the coulomb correction factor by a maximum of only 0.1%. For the QE region, the factor changes by a maximum of 0.2% for Carbon, 0.4% for Aluminum, 0.7% for Iron, and 1.0% for Lead. Although there is some Bjorken-X dependence to the amount the correction factor changes, the changes are correlated. So, we just choose to conservatively use the maximum change for each target as a normalization uncertainty.

Following previous results [30, 31], we place a conservative 0.5% point-to-point uncertainty on the bin centering correction factor.

6.3.5 Bin Migration

The data in this analysis are binned in Bjorken-X. Since the cross-section and the Bjorken-X reconstruction resolution vary significantly across the range of the analysis, it is important to study the effects of bin migration. We perform this study using the *CLAS* monte-carlo simulation.

In figure 6.5, we show the resolution on Bjorken-X for events generated in different Bjorken-X ranges. The plots cover the lower range of the QE analysis region. As can be seen, the resolution becomes worse with increasing Bjorken-X. This trend continues to larger Bjorken-X values and down to the DIS region. In the DIS case, the resolution is much better than our chosen bin size of 0.04, and the cross-sections do not vary as rapidly with Bjorken-X (figure 5.7).
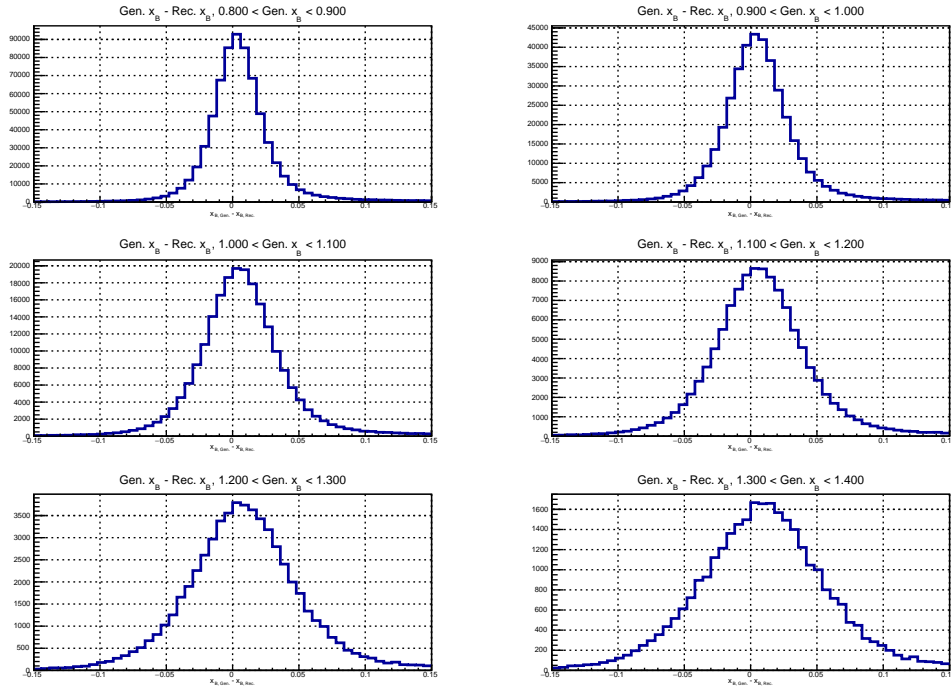

Figure 6.5: Resolutions for Bjorken-X from 0.8-1.4 determined from the simulation.

In the QE region, however, the cross-sections fall quickly with increasing Bjorken-X (figure 5.8), and the resolution degrades. To study the effect of this, we generate events from both the solid and liquid vertex uniformly

in energy and solid angle and weight the events with our QE cross-section model. We know that this model describes the shape of our distribution well (section 5.2). In figure 6.6, we bin the weighted simulation as in data; the blue curve represents the number of events generated in a given bin; the green curve represents the number of events generated in a given bin that are accepted (but they may be reconstructed in any bin); the red curve is the number of events reconstructed in a given bin. The experimental data provides us with the equivalent of the red curve. So, the relevant quantity for understanding bin migration is the ratio of the green to the red curve in every bin.
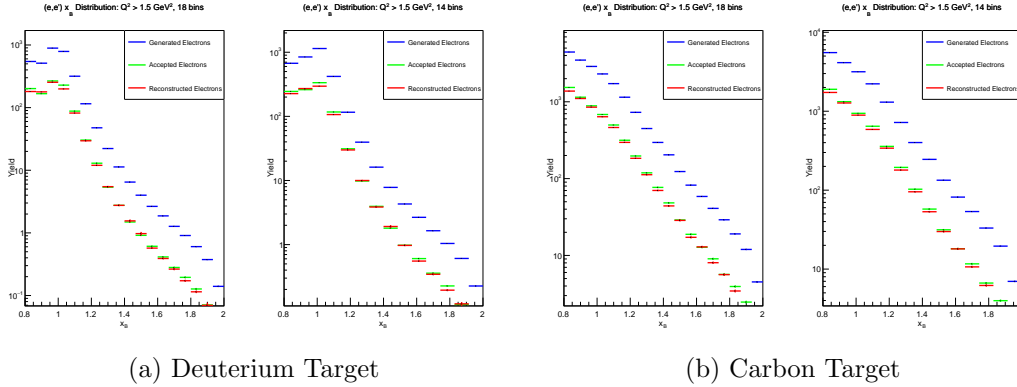

(a) Deuterium Target   (b) Carbon Target

Figure 6.6: Number of weighted QE simulated events generated, accepted, and reconstructed in each X_B bin. We show two different bin widths here; the larger bin widths are used in the final analysis and in plots 6.7 and 6.8.

In figure 6.7, we show this ratio for events generated from the Deuterium target and weighted by the Deuterium model cross-section, for events generated from the solid target and weighed by either the Carbon or Lead model cross-section. The values seem to be consistent between the solid and Deuterium targets, which indicates that bin migration effects should largely cancel in the ratio. To quantify the effect, we take the ratio of the Carbon to Deuterium points in 6.7. This ratio is shown in figure 6.8. We take a weighted mean of the ratios to put a 1.7% point-to-point uncertainty due to bin migration.
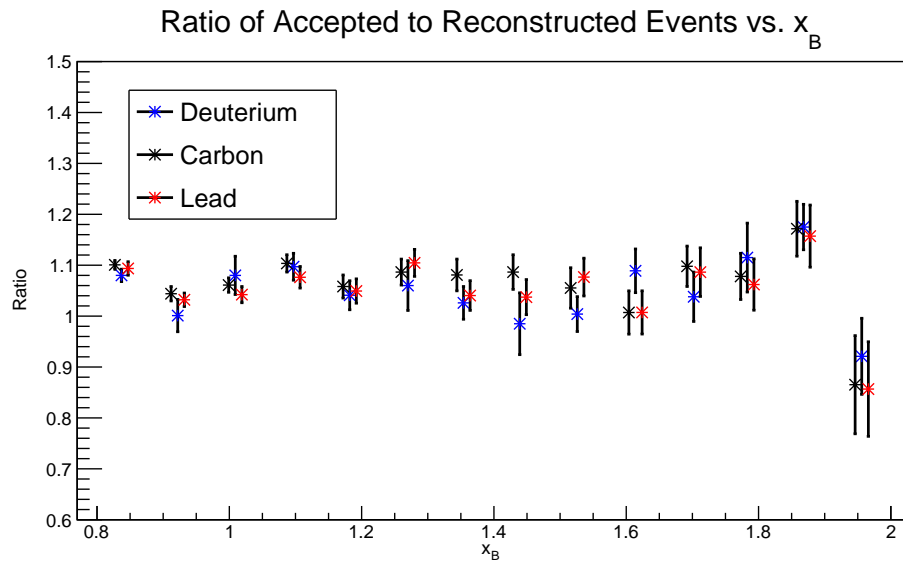
Figure 6.7: Ratio of Green to Red curves in figure 6.6. The Carbon and Lead values were produced by using the exact same simulated events and weighting them by their respective model cross-sections.
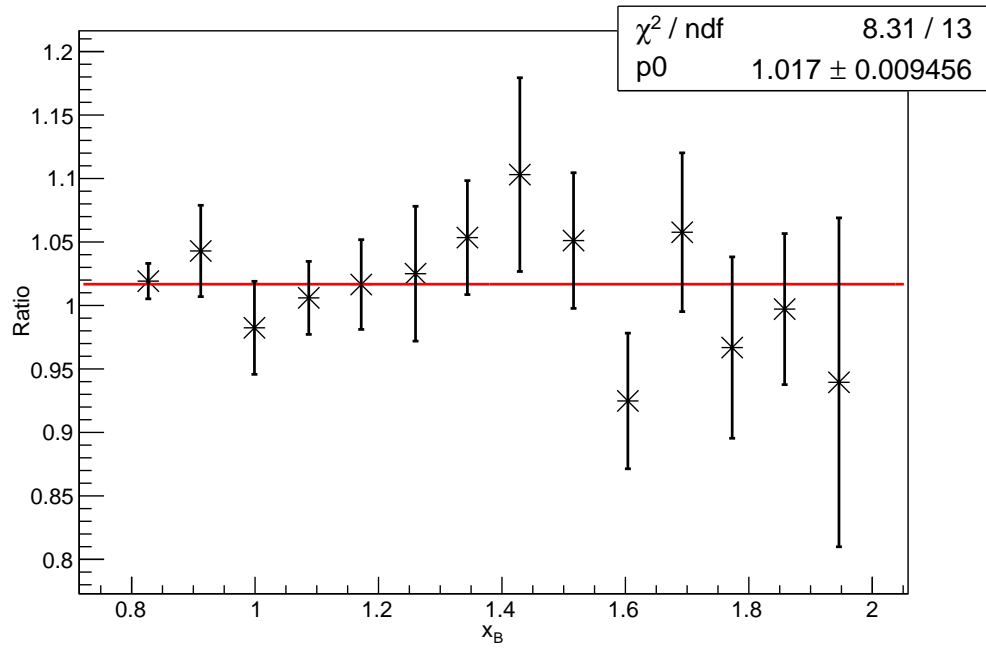
Figure 6.8: Ratio of the Carbon to Deuterium points in figure 6.7. We take a weighted mean of the points here to quantify the uncertainty.

6.3.6 Kinematic Corrections

For the QE case, we estimated the maximum amount that the electron momentum may be reconstructed incorrectly in section 3.3.2. To check the effect of this potential mis-reconstruction on the cross-section ratios, we look at how much every measured cross-section ratio changes if we shift the momentum by 20 MeV/c. We find that the ratio changes between 0.2-0.3%. So, we place a point-to-point uncertainty of 0.3% on all bins. We do not apply any uncertainty on the applied polar angle corrections.

For the DIS case, we applied momentum and polar angle corrections. We do not place any uncertainty on these corrections.

Bibliography

[1] O. Hen *et al.*, *Int. J. Mod. Phys. E* **22**, 1330017 (2013),

[2] S. Malace, D. Gaskell, D.W. Higinbotham, I. Cloet, *Int. J. Mod. Phys. E* **23**, 1430013 (2014),

[3] N. Fomin, D. Higinbotham, M. Sargsian, and P. Solvignon, New Results on Short-Range Correlations in Nuclei,

[4] L. B. Weinstein *et al.*, *Phys. Rev. Lett.* **106**, 052301 (2011).

[5] O. Hen, E. Piasetzky, and L. B. Weinstein, *Phys. Rev. C* **85**, 047301 (2012).

[6] L. B. Weinstein and S.E. Kuhn, *Short Distance Structure of Nuclei: Mining the Wealth of Existing Jefferson Lab Data, L.B. Weinstein and S.E. Kuhn*, DOE Grant DE-SC0006801

[7] W. K. Brooks *et al.*,*Quark propagation through cold QCD matter*, Proposal to PAC22 (2002).

[8] K. Hafidi *et al.*, Q^2 *dependence of nuclear transparencies for incoherent ρ^0 electroproduction*, Proposal to PAC22 (2002).

[9] H. Hakobyan *et al.*, *Nucl. Instr. and Meth. A* **592**, 218-223 (2008).

[10] L. El Fassi *et al.*, *Search for the Onset of Color Transparency via ρ^0 Electroproduction off Nuclei*, approved CLAS analysis note (2011).

[11] O. Hen *et al.*,*Probing PP-SRC in ^{12}C, ^{27}Al,^{56}Fe, and ^{208}Pb Using the A(e,e'p) an A(e,e'pp) Reactions*, approved CLAS analysis note (2013).

[12] N. Baltzell and S. Stepanyan. *Beam XY-Position at the Target for CLAS/EG6*, CLAS note 2013-007.

[13] D. Protopopescu *et al.*, *Electron Momentum Corrections for CLAS at 4.4 GeV*, CLAS Note 2001-008.

[14] S. Stepanyan, *Beam energy measurement with $ep \rightarrow ep$ elastic scattering on CLAS*. CLAS Note 2002-008.

[15] K. Y. Kim *et al.*, *General momentum correction for for CLAS...* , CLAS Note 2001-018.

[16] A. Klimenko and S. Kuhn, *Momentum Corrections for E6*, CLAS Note 2003-005.

[17] M. Ungaro, *π^0 electroproduction from $\Delta(1232)$ at high momentum transferred with CLAS*, PhD thesis (2005).

[18] V. Burkert, L. Elouadrhiri, S. Stepanyan, *Deep Virtual Compton Scattering with CLAS*, CLAS Note 2001-006.

[19] Douglas Higinbotham and Stepan Stepanyan, Private communication.

[20] L. W. Mo and Y.S. Tsai, *Rev. Mod. Phys.* **41** 205 (1969).

[21] `SIMC Monte Carlo`.

[22] Reynier Cruz Torres, Private communication.

[23] M. Sargsyan, *Computer Code for Inclusive (ee') Electro-production Reactions and Radiative Corrections*, CLAS Note 90-007.

[24] A. Aste and J. Jourdan, *Europhys. Lett.* **67**, (2004) 753-759.

[25] P. Solvignon, D. Gaskell, and J. Arrington, `arXiv:0906.0512` [nucl-ex].

[26] J. Gomez *et al.*, *Phys. Rev. D* **49**, 4348 (1994).

[27] J. Seely *et al.*, *Phys. Rev. Lett.* **103**, 202301 (2009).

[28] N. Fomin *et al.*, *Phys. Rev. Lett. 108*, 092502 (2012).

[29] X. Zheng, *Cryogenic Target Thickness Study for EG2* (http://www.jlab.org/ xiaochao/eg2/eg2targ.ps), (2003).

[30] N. Fomin, *Inclusive electron scattering from nuclei at $x > 1$ and high Q^2 with a 5.75 GeV beam*, PhD thesis (2008).

[31] A. Daniel, *Precise Measurement of the Nuclear Dependence of the EMC Effect at Large x*, PhD thesis (2007).